

ADVANCED MATERIALS

Supporting Information

for *Adv. Mater.*, DOI 10.1002/adma.202211742

Chloride-Based Additive Engineering for Efficient and Stable Wide-Bandgap Perovskite Solar Cells

*Xinyi Shen, Benjamin M. Gallant, Philippe Holzhey, Joel A. Smith, Karim A. Elmestekawy, Zhongcheng Yuan, P. V. G. M. Rathnayake, Stefano Bernardi, Akash Dasgupta, Ernestas Kasparavicius, Tadas Malinauskas, Pietro Caprioglio, Oleksandra Shargaieva, Yen-Hung Lin, Melissa M. McCarthy, Eva Unger, Vytautas Getautis, Asaph Widmer-Cooper, Laura M. Herz and Henry J. Snaith**

Supporting Information for:

Chloride-based additive engineering for efficient and stable wide-bandgap perovskite solar cells

Xinyi Shen¹, Benjamin M. Gallant¹, Philippe Holzhey¹, Joel A. Smith¹, Karim A. Elmestekawy¹, Zhongcheng Yuan¹, P. V. G. M. Rathnayake³, Stefano Bernardi³, Akash Dasgupta¹, Ernestas Kasparavicius⁵, Tadas Malinauskas⁶, Pietro Caprioglio¹, Oleksandra Shargaieva⁷, Yen-Hung Lin¹, Melissa M. McCarthy¹, Eva Unger^{7,8}, Vytautas Getautis⁶, Asaph Widmer-Cooper^{3,4}, Laura M. Herz^{1,2}, Henry J. Snaith^{1}*

¹ Clarendon Laboratory, Department of Physics, University of Oxford, Parks Road, Oxford, OX1 3PU, United Kingdom

² Institute for Advanced Study, TU Munich, Lichtenbergstr. 2a, 85748 Garching, Germany

³ ARC Centre of Excellence in Exciton Science, School of Chemistry, University of Sydney, Sydney, New South Wales 2006, Australia.

⁴ The University of Sydney Nano Institute, University of Sydney, Sydney, New South Wales 2006, Australia.

⁵ Department of Molecular Compound Physics, Centre for Physical Sciences and Technology, Sauletekio Avenue 3, Vilnius LT-10257, Lithuania

⁶ Department of Organic Chemistry, Kaunas University of Technology, Kaunas LT-50254, Lithuania.

⁷ Young Investigator Group Hybrid Materials Formation and Scaling, Helmholtz-Zentrum Berlin für Materialien und Energie GmbH, 14109 Berlin, Germany

⁸ Chemical Physics and NanoLund, Lund University, Lund, Sweden.

Materials

Indium tin oxide-coated glass substrates (ITO, 15 Ω cm⁻², AMG), lead(II) iodide (PbI₂, 99.99%, trace metal basis, Tokyo Chemical Industries), lead(II) bromide (PbBr₂, > 98+%, Alfa-Aesar), lead(II) chloride (PbCl₂, 99.999%, trace metal basis, Sigma Aldrich), formamidinium iodide (FAI, > 99.99%, Greatcell Solar Materials), cesium iodide (CsI, 99.9% (metal basis), Alfa-Aesar), methylamine hydrochloride (MAcI, 99.99%, Xi'an Polymer Light Technology Corp.), poly[bis(4-phenyl)(2,4,6-trimethylphenyl)amine] (PTAA, Xi'an Polymer Light Technology Corp.), self-assembled monolayers (SAMs, including [2-(9H-Carbazol-9-yl)ethyl]phosphonic acid (2PACz, Tokyo Chemical Industry), [2-(3,6-Dimethoxy-9H-carbazol-9-

yl)ethyl]phosphonic acid (MeO-2PACz, Tokyo Chemical Industry), and [4-(3,6-dimethyl-9H-carbazol-9-yl)butyl]phosphonic acid (Me-4PACz, Tokyo Chemical Industry)), aluminium oxide nanoparticles (Al_2O_3 , < 50 nm particle size, 20 wt.% in isopropanol, Sigma Aldrich), Fullerene- C_{60} (C_{60} , 99.5%, Sigma Aldrich), bathocuproine (BCP, 98%, Alfa-Aesar), silver pellets (Ag, 99.999%, Kurt J. Lesker Company), gold pellets (Ag, 99.999%, Kurt J. Lesker Company).

Ethanol (anhydrous, $\geq 99.9\%$, VWR), toluene (anhydrous, 99.8%, Sigma Aldrich), 2-propanol (IPA, anhydrous, 99.5%, Sigma Aldrich), N,N-dimethylformamide (DMF, anhydrous, 98%, Sigma Aldrich), dimethyl sulfoxide (DMSO, anhydrous, 98%, Sigma Aldrich), anisole (anhydrous, 99.7%, Sigma Aldrich), methyl acetate (anhydrous, 99.5%, Sigma Aldrich).

In this work, all powders were used as purchased without further purification and weighed in a nitrogen-filled glovebox without exposure to light.

Device Fabrication

ITO-coated glass substrates were cleaned prior to use by 15-minute sonication in deionised (DI) water with Decon90 (2 vol%) cleaning detergent, followed by scrubbing with a toothbrush to get rid of stains and dusts, before being rinsed and sonicated in DI water, acetone and IPA for 15 minutes sequentially. The substrates were then dried with a nitrogen gun followed by an UV-ozone treatment (15 minutes for PTAA and 30 minutes for SAMs). Immediately after the substrate preparation was complete, the substrates were transferred into a N_2 -filled glovebox, and the hole transport layer was deposited.

For reference devices, PTAA solution (80 μL , 1.5 mg mL^{-1} in toluene) was dispensed onto a substrate statically. The substrate was spinning at 6000 rpm (3 seconds ramp time) for 30 seconds, and then annealed at 100 °C for 10 minutes. For optimised devices, SAMs were used instead of PTAA, SAM solutions (100 μL , 0.3 mg mL^{-1} of 2PACz, MeO-2PACz or Me-4PACz in anhydrous ethanol) were dropped onto a substrate statically. After 5 seconds to help the solution spread, the substrate was spinning at 3000 rpm (6 seconds ramp time) for 30 seconds, and then annealed at 100 °C for 10 minutes. The surface of PTAA and SAMs films were very hydrophobic,

hence Al₂O₃ nanoparticles (1:150 vol% in IPA) were spin coated dynamically on top at 2000 rpm for 20 seconds as a wetting agent.

PbI₂, PbBr₂, FAI, CsI were weighed stoichiometrically in a N₂-filled glove box to the target perovskite composition (e.g. FA_{0.83}Cs_{0.17}Pb(I_{0.6}Br_{0.4})₃). To form the precursor solution, DMF:DMSO mixture (4:1 volume ratio) was added to achieve a concentration of 1.2 M. To make FA_{0.83}Cs_{0.17}Pb(I_{0.6}Br_{0.4})₃ solutions with MACl additives, excess molar (0-45 mol%) of MACl was added into the precursor as additives. The precursor solutions were agitated until all solids were fully dissolved. Perovskite precursor solution (170 μL) was dispensed dynamically onto a substrate spinning at 1000 rpm. The substrate was accelerated to 5000 rpm over the course of 5 seconds and remained at this speed for 35 seconds. 5 seconds before the end of this process, anisole (325 μL) was applied to the spinning substrate as an anti-solvent quench. For devices with no MACl additives, the films were then annealed at 100 °C for 30 minutes in a N₂-filled glovebox. For devices with MACl additives, the substrates were transferred out of the glovebox and annealed at 150 °C for 10 minutes under ambient atmosphere (relative humidity (RH) ~ 30%). The annealed substrates were allowed to cool down, then transferred back into a N₂-filled glovebox and loaded into a thermal evaporator.

C₆₀ (30 nm) was deposited on top of the perovskite active layer via thermal evaporation under vacuum (~ 3E-6 torr) with no masks applied. After completing the evaporation, BCP solution (100 μL, 0.5 mg/mL in IPA) was applied onto a substrate spinning at 5000 rpm for 30 seconds followed by annealing at 100 °C for 1 minute to remove any remaining solvent.

Finally, the devices were completed by thermally evaporating silver (100 nm) through shadow masks (active area defined as 0.25 cm² or 1 cm²) at an initial rate of 0.2 A s⁻¹ (ramped up to 1 A s⁻¹ in 20 min) under high vacuum (~10⁻⁶ torr) using a thermal evaporator (Nano36, Kurt J. Lesker). The devices for photo and thermal stability test used gold (80 nm) electrodes instead of silver.

For the triple halide devices demonstrated in the **Supplementary Figure 34 & 35**, Me-4PACz, Al₂O₃ nanoparticles, C₆₀, BCP and Ag were deposited as described above. For the active layer, FA_{0.75}Cs_{0.25}Pb(I_{0.7}Br_{0.3})₃ precursor (1.4 M) with PbCl₂ (10 mol% excess) and MACl (10 mol% excess) additives was used instead to achieve the target

composition ($E_g = 1.8$ eV) as described in literature.^[1] Perovskite precursor solution (175 μ L) was spin-coated dynamically on top of the hole transport layer at 5000 rpm for 35 seconds. 25 seconds before the end of this process, methyl acetate (200 μ L) was applied to the spinning substrate as an anti-solvent quench. The substrates were then annealed at 100 °C for 30 minutes in a N₂-filled glovebox.

Characterisation

Ultraviolet-Visible (UV-Vis) Absorption Spectroscopy

Reflectance and transmittance spectra were recorded on a Varian Cary 1050 UV-Vis spectrophotometer equipped with an integrating sphere. From these measurements, in combination with the photoactive layer thickness, absorption coefficients were calculated assuming a direct bandgap semi-conductor. Separately, absorbance spectra were measured with a Varian Cary 300 Bio UV-Visible spectrophotometer with a 50x50 mm reflective neutral density filters with an optical density of 3.0 (made out of UV fused silica).

X-ray Diffraction (XRD)

The 1D-XRD patterns were obtained with a Panalytical X'Pert Pro X-Ray diffractometer and 2D-XRD patterns using a Rigaku SmartLab X-ray diffractometer and a HyPix-3000 2D hybrid pixel array detector, both with a CuK α 1 (1.54060 Å) source. An Anton Paar DCS-350 heating stage was employed in conjunction with the Rigaku SmartLab diffractometer for relevant measurements.

Grazing-Incidence Wide-Angle X-ray Scattering (GIWAX)

In situ GIWAXS measurements were conducted at the mySpot beamline at the BESSY II synchrotron. Solutions were prepared according to the methods above, before blade coating with a film thickness of ~ 20 μ m and then immediately transferred into a sealed chamber. Films were then measured while drying, from room temperature to 100 °C controlled with an integrated hotplate and under a flow of N₂ to emulate quenching. The synchrotron beam with an energy of 9 keV ($\lambda = 1.378$ Å) was incident at an angle of 2°, and the diameter of the beam was ~100 μ m.^[2] Scattering was collected in 2 s increments using an Eiger 9M (DECTRIS) hybrid photon counting detector at a

distance of 320 mm, with the geometry calibrated using LaB6 as the calibrant. Detector images were then resampled into Q-space and azimuthally integrated using scripts based on the PyFAI and pygix libraries.^[3,4]

Scanning Electron Microscopy (SEM)

A FEI Quanta 600 FEG Environmental Scanning Electron Microscope (ESEM) was employed to investigate perovskite layer morphology. Accelerating voltages between 4-15 kV were employed for various analysis.

Nuclear Magnetic Resonance (NMR) Spectroscopy

A two-channel Bruker AVANCE III HD Nanobay 400 MHz instrument running TOPSPIN 3 equipped with a 5 mm z-gradient broadband/fluorine observation probe is used. The signal from residual non-deuterated DMSO solvent is used for reference.

Characterisation of Solar Cells

Current-voltage (J - V) and maximum power point (MPP) measurements were measured (2400 series source meter, Keithley Instruments) in ambient air under both light (simulated AM 1.5 irradiance generated by a Wavelabs SINUS-220 simulator) and in the dark. The active area of the solar cell was masked with a black-anodised metal aperture to either 0.25 or 1.00 cm², within a light-tight holder. For each device, the PV metrics were obtained in the following sequence. Firstly, the devices were kept at open-circuit condition under illumination for 6 seconds until the fluctuations in readings were nearly negligible to obtain the steady-state V_{OC} . Then a 'reverse' J - V scan (from open-circuit to short-circuit) and a 'forward' J - V scan (from short-circuit to forward bias) were measured both at a scan rate of 245 mV s⁻¹. Subsequently, active MPP tracking measurements using a gradient descent algorithm were performed for 30 s to obtain the η_{mpp} . Lastly, the devices were kept at short-circuit condition under illumination for 3 seconds until the fluctuations in readings were nearly negligible to obtain the steady-state J_{SC} . The intensity of the solar simulator was set periodically such that the short-circuit current density from a KG3-filtered Si reference photodiode (Fraunhofer ISE) matched its 1-sun certified value. A local measurement of the intensity before each batch of solar cell measurements were performed, was made by integrating the spectrum obtained from the solar simulator's internal spectrometer. By taking the ratio of this internal intensity measurement to one obtained at the time of

calibration we determined the equivalent irradiance at the time of measurement. For the data presented in this publication, this gave values ranging from 0.985-1.005 suns equivalent, which have been applied to the calculation of power conversion efficiencies for each individual measurement.

Photoluminescence Quantum Efficiency Measurement

Photoluminescence quantum efficiency measurements were acquired using a custom built PLQE setup in an integrating sphere. Samples were photoexcited using a 405 nm laser (laser power = 5.86 mW). The PL was collected using a high-resolution monochromator and hybrid photomultiplier detector assembly (PMA Hybrid 40, PicoQuant GmbH). The PLQE were extracted from the photon energy (hf), photon numbers of the excitation and emission obtained from numerical integration using Python.

Steady-state photoluminescence

A 398 nm diode laser (PicoHarp, LDH-D-C-405M) was used to photo-excite the samples, on a continuous wave setting at an intensity of 5800 mW/cm^2 . The resultant PL was collected and coupled into a grating spectrometer (Princeton Instruments, SP-2558), which directed the spectrally dispersed PL onto a silicon iCCD (intensified charge coupled device, PI-MAX4, Princeton Instruments). The samples were mounted in a vacuum cell under low pressure ($\sim 10^{-2}$ mbar).

AM1.5 equivalent photon flux

The AM1.5 equivalent intensity is estimated to be the equivalent laser intensity that photogenerates the same density of charge carriers within the film as would be under the AM1.5 solar spectrum. Due to the sharp absorption onset and high values of the absorption coefficient of these films, we expect light penetration through the film to be much shorter than its thickness, and it can be assumed that all incident photons with energies higher than the bandgap to be entirely absorbed. Accordingly, the AM1.5 equivalent intensity would correspond to a laser intensity that results in the same incident photon flux as the AM1.5 solar spectrum from the above-bandgap photons.

The bandgap of the wide-bandgap mixed phase perovskite is measured to be at 677 nm from the steady-state PL measurements (reference to SSPL figure), and integrating over the spectral photon flux from the AM1.5 solar spectrum, expressed as:

$$AM1.5(\lambda) \cdot \left(\frac{hc}{\lambda}\right)^{-1} \cdot d\lambda,$$

from $\lambda = 0$ nm to $\lambda = 677$ nm, reveals that there are 1×10^{21} photons per second per meters squared incident on our samples under an AM1.5 solar spectrum.

Therefore, an AM1.5 equivalent intensity corresponds to an intensity of 50 mW/cm² from a 398 nm laser with an effective illumination area of 2.97×10^{-4} cm², while a 5800 mW/cm² laser intensity would correspond to around 115 times an AM1.5 equivalent intensity.

Time-resolved photoluminescence

TRPL of the thin films was measured using TCSPC (time-correlated single photon counting) following excitation by a 398 nm picosecond pulsed diode laser at a repetition rate of 2.5 MHz (PicoHarp, LDH-D-C-405M). The resultant PL was collected and coupled into a grating spectrometer (Princeton Instruments, SP-2558), which directed the spectrally dispersed PL onto a photon-counting detector (PDM series from MPD), whose timing was controlled with a PicoHarp300 TCSPC event timer.

External Quantum Efficiency

External quantum efficiency (EQE) measurements were performed using a custom-built set up based on a Bruker Vertex 80v Fourier transform interferometer. The solar cells were illuminated with a 250 W quartz-tungsten halogen lamp that was first passed through a monochromator (Princeton Instruments SP2150) with a filter wheel (Princeton Instruments FA2448), then chopped with an optical chopper (Thorlabs MC2000B) at 280Hz, and finally focussed onto the sample with a smaller spot size than the solar cell area (as defined by the metallic top contact). The amplitude of the resulting AC current signal was measured with a lock-in amplifier (Stanford Research Systems SR830) as the voltage drop across a 50 Ohm resistor in series with the solar cell. To determine the EQE, the photocurrent spectrum of the device under test was divided by that of a calibrated Si reference cell (Thorlabs FDS100-CAL) of a known EQE. Device active areas were masked with a black-anodised metal aperture, having an active area of either 0.25 cm² or 1.00 cm².

Potential of mean force calculations

Molecular Dynamics (MD) simulations were performed using the AMOEBA polarizable force field with the OpenMM package.^[5] Unaltered AMOEBA09 parameters were used for DMF, DMSO, Cl⁻, Br⁻ and I⁻, while the Pb²⁺ parameters, developed and tested for solid perovskites and their precursors in solution, were taken from literature.^[6] Initial equilibrations were performed in the NPT ensemble at 1 atm and 300 K using an Andersen thermostat and a Monte Carlo barostat with a leap-frog Verlet integrator with 1 fs timestep. The non-bonding cutoffs was set to 12 Å. Periodic Boundary Conditions and the Particle Mesh Ewald (PME) method were used. Mutual polarization was imposed with 10⁻⁵ tolerance.

Constrained MD simulations were used to calculate the potential of mean force (PMF) as a function of the lead-halide ion separation, using simulation boxes containing 500 solvent molecules (DMF or DMSO). Simulations were performed at Pb–X separations (in Angstroms) of 2.6–4.6 (in increments of 0.1), 4.8–6.8 (in increments of 0.2), 7.0–12.5 (in increments of 0.5), and 13–16 (in increments of 1). When adding the second halide ion, a loose harmonic spring [$K = 1.2$ (kcal/mol)/Å²] was used to keep the first ion bonded to lead, with the equilibrium bond lengths taken from crystallographic data; 3.12, 2.96 and 2.84 Å for Pb–I, Pb–Br and Pb–Cl, respectively. An NVT simulation of 2 ns was performed for each value of the reaction coordinate, with the last 1.2 ns used to calculate the PMF. The free energy difference, $\Delta F(z_s)$, between a state where the halide ion is positioned at z_s and a reference state where the halide ion is at z_0 is given by equation below,

$$\Delta F(z_s) = F(z_s) - F_0 = - \int_{z_0}^{z_s} \langle f_z(z'_s) \rangle dz'_s,$$

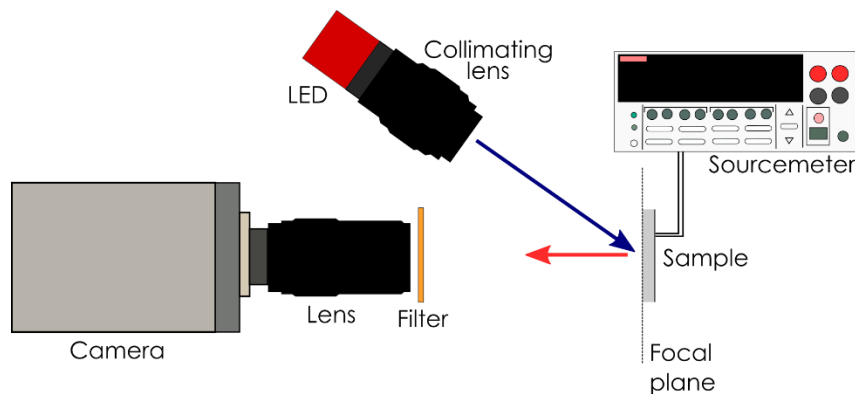
where $f_z(z'_s)$ is the z component of the force exerted by the solvent and lead ion on the halide ion at the position z'_s . The average forces at each step were then interpolated and integrated to obtain the PMF.^[7]

Visible Light Microscopy

Optical microscope images were taken on a Nikon Eclipse LV100ND microscope with Nikon TU Plan Fluor lenses (10x/0.30 A, 20x/0.45 A, 50x/0.60 B, 100x/0.90 A). The images are taken with an attached Nikon Digital Camera D6.10.

Quasi-Fermi Level Splitting (QFLS) Mapping

The spatially resolved data (QFLS maps) were taken using an in house-built photoluminescence measurement setup. The setup consists of an LED illumination source, an image sensor and lens (camera) to collect and measure the photoluminescence (PL), a longpass filter to prevent stray/reflected light from the excitation source from falling onto the image sensor, and a source meter to bias the sample.



The illumination was provided by a ThorLabs M450LP1 LED collimated by a Thorlabs SM2F lens. The emission was at 450 nm, well above the bandgap of the tested samples. The Intensity was controlled by controlling the power supplied to the LED. In order to determine the '1 sun' illumination, the sample was shorted and the LED power tweaked till the current readout was near the short circuit current measured on a solar simulator. The biasing was done using a Keithley 2400.

The PL was measured using an ANDOR Zyla 4.2, a 'scientific CMOS' or sCMOS sensor. The sensor was cooled to 0C. The collection lens was a Kowa LM50XC, a 50 mm lens with an aperture of f2.0. The sample was brought to the focal plane of the lens, and positioned to coincide with the center of the incident beam. The filter was a Thorlabs FGL515S longpass filter, with a cut off of 515 nm. Exposure times were

varied to obtain a good signal. In the analysis, the measured counts were linearly scaled by exposure time to correct for this.

In order to both correct for beam nonuniformity as well as calculating the PLQY for the QFLS calculation, a white reference was imaged without the filter. This was a barium sulphate plate, which has near unity reflectivity and a Lambertian reflection profile. This gave both a spatial map of the beam that could be used to correct the PL images, as well as the measured counts corresponding to the photon flux from the LED, at some known intensity and exposure time. The

$$PLQY = \frac{\text{Counts from sample}}{\text{Counts from LED}} \times C,$$

on a per pixel level, where C is a correction factor determined to account for:

- The LED intensity difference between the sample and the ref images
- The Quantum efficiency of the detector and wavelength response of the lens and filter.

The quasi-Fermi level splitting (QFLS) was determined in-line with our previous work.^[8,9] In brief, we calculate the $QFLS$ according to

$$QFLS = k_B T \ln \left(PLQE \cdot \frac{J_G}{J_{0,rad}} \right),$$

where k_B is the Boltzmann constant, T the absolute temperature, $PLQE$ is the photoluminescence quantum efficiency, J_G is the generation current and $J_{0,rad}$ is the radiative recombination current in the dark. The generation current can be calculated according to

$$J_G = q \int_0^\infty d\lambda EQE(\lambda) \varphi_{AM1.5}(\lambda),$$

where q is the elementary charge, EQE is the photovoltaic external quantum efficiency and $\varphi_{AM1.5}$ is the solar photon flux. In a similar manner, one calculates $J_{0,rad}$ as

$$J_{0,rad} = q \int_0^\infty d\lambda EQE(\lambda) \varphi_{BB}(\lambda),$$

with φ_{BB} being the blackbody spectrum at room temperature. In our calculation, following the Shockley-Queisser approach, we estimated a $QFLS_{rad}$ by assuming a step function absorption profile instead of the EQE_{PV} .

From that, the radiative limit of the $QFLS$ ($QFLS_{rad}$) (PLQE = 100%) can be calculated with the following equation:

$$QFLS_{rad} = k_B T \ln \left(1 + \frac{J_G}{J_{0,rad}} \right),$$

In this case, we approximated J_G to short circuit current J_{SC} and used the room temperature where $T = 298$ K. As such we calculated the $QFLS_{rad}$ of our perovskite absorber as

$$QFLS_{rad} = k_B T \ln \left(1 + \frac{J_{SC}}{J_{0,rad}} \right) = 1.484 \text{ eV for } E_g = 1.77 \text{ eV or } 1.512 \text{ eV for } E_g = 1.8 \text{ eV}.$$

Finally, we calculated our QFLS as follows

$$QFLS = QFLS_{rad} + k_B T \ln(PLQE).$$

Wavelength Dispersive X-Ray Fluorescence (WDXRF)

The atomic percentages of the halide and lead atoms in the perovskite thin films were determined using wavelength dispersive X-Ray Fluorescence (WDXRF). Measurements were performed on a WDXRF with a Rh-tube at room temperature. The angle between the XRF detector and incident X-ray beam is fixed to 90° . The angle between the normal to the sample surface and the incident X-ray beam was 15° , optimized to reduce self-absorption effects in the XRF signal while minimizing the footprint of the X-ray beam. The X-Ray beam entered the substrate through the perovskite side. From the XRF, we identify the elements in the film according to their characteristic fluorescence energy. Atomic percentages were determined using the fundamental parameters method.^[10]

Photo and Thermal Stability

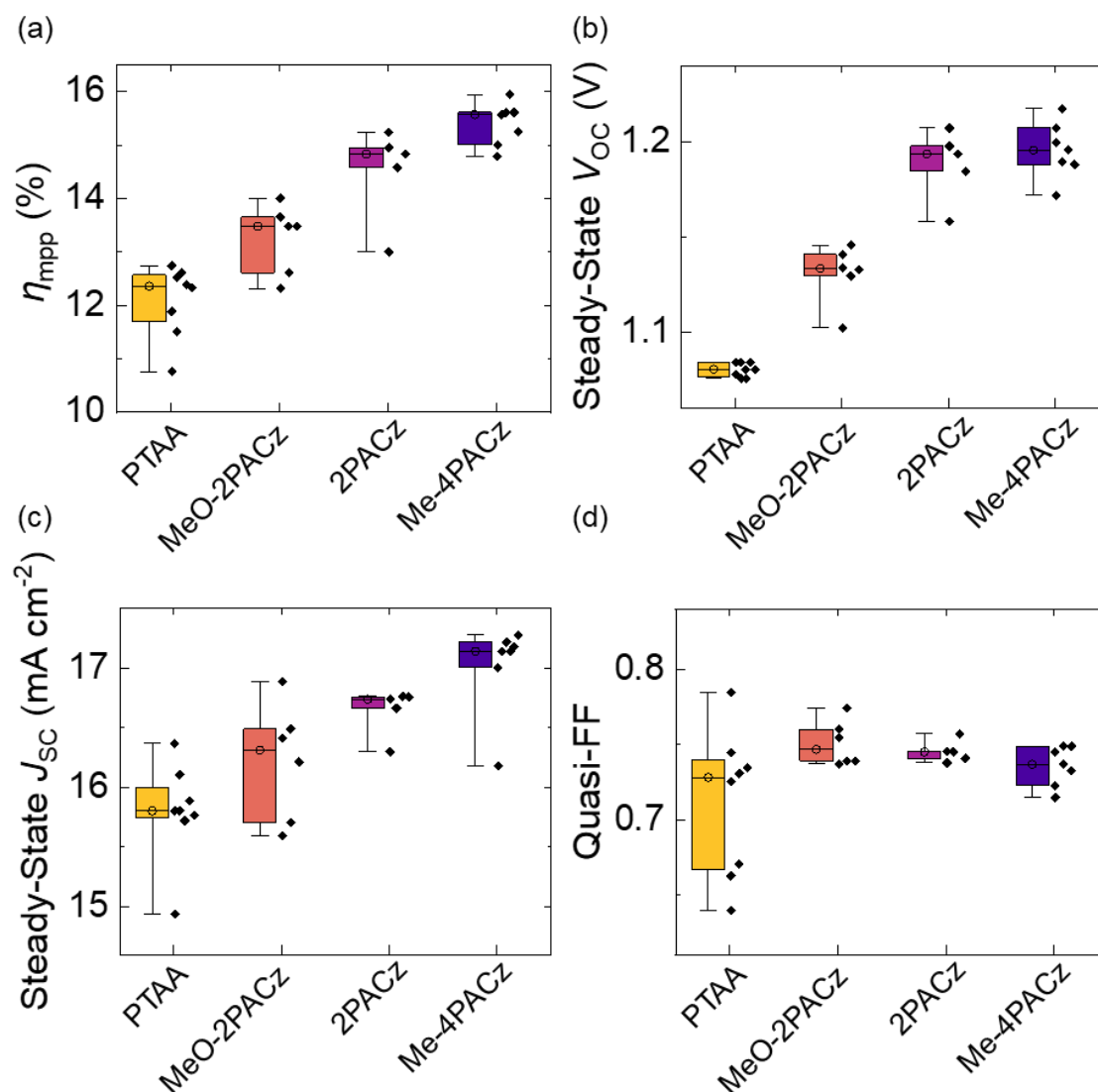
Photo and thermal stability measurements were carried out on encapsulated devices in a light-soaking aging box with continuous illumination of intensity equivalent to 1-sun illumination. The devices were kept at open-circuit condition, 65°C in air (RH ~ 50%).

Thermal Stability

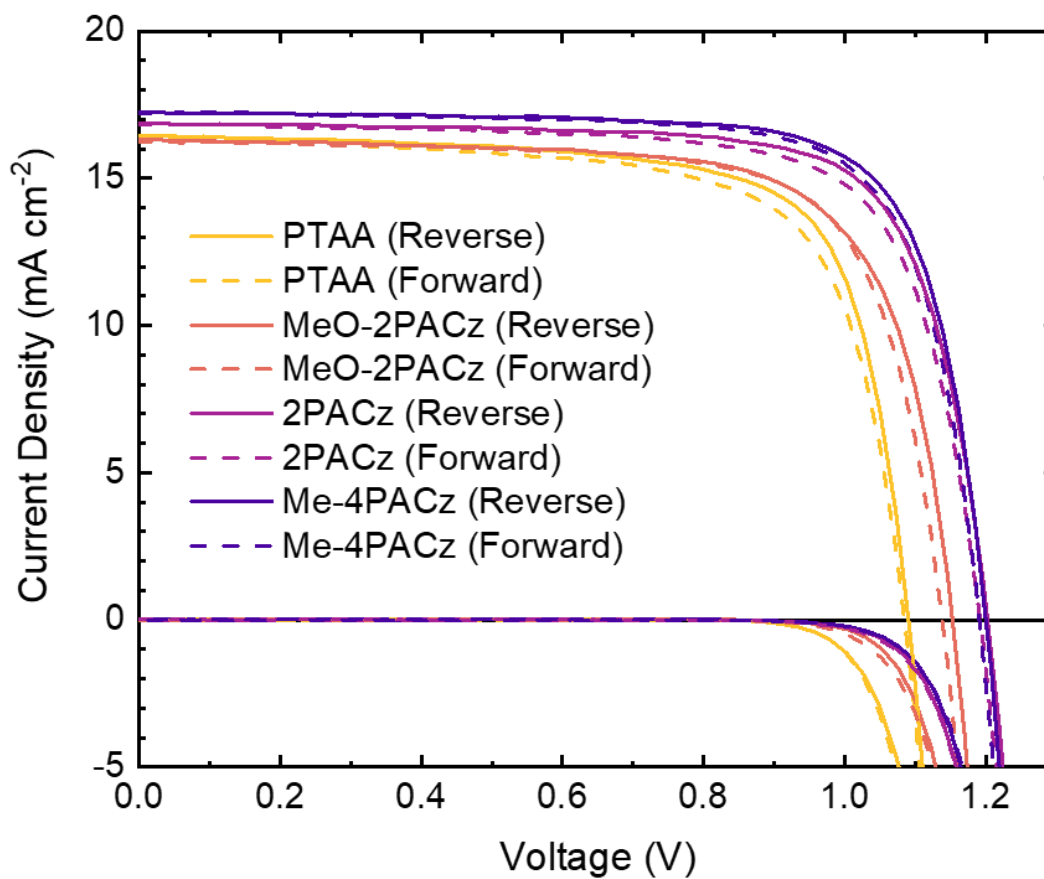
Thermal stability measurements were carried out on unencapsulated devices in an oven with a real-time temperature controller. The devices were kept at open-circuit condition, 85 °C in N₂, in dark.

Supplementary note 1

Self-assembled monolayers (SAMs) have previously been shown to reduce the V_{oc} deficit and suppress halide segregation in p-i-n perovskite-silicon tandem solar cells via mitigating non-radiative losses and improving hole extraction.^[11–13] Here we compare the three most used SAM molecules ([2-(9H-Carbazol-9-yl)ethyl]phosphonic acid (2PACz), [2-(3,6-Dimethoxy-9H-carbazol-9-yl)ethyl]phosphonic acid (MeO-2PACz) and Me-4PACz) with PTAA for our control composition $FA_{0.83}Cs_{0.17}Pb(I_{0.6}Br_{0.4})_3$ ($E_g = 1.77$ eV) in p-i-n PSCs. As we show in **Supplementary Figure 1 and 2**, all three SAMs lead to enhancements in photovoltaic (PV) performance, especially in V_{oc} and short-circuit current density (J_{sc}). Of these SAMs, Me-4PACz provides the most substantial improvement in the device performance. Of particular note is the difference in steady-state V_{oc} between Me-4PACz and PTAA, which is as large as 140 meV in the champion cells. To investigate this performance boost, we conduct external quantum efficiency (EQE) measurements on full devices based on the different HTLs (**Supplementary Figure 3**). The integrated current density values extracted from the EQE measurements are in good agreement with the J_{sc} values obtained from the current-voltage (J - V) characteristics (**Supplementary Table 1**). We interpret the overall increase in EQE over a wide range of photon energies (1.8 – 3.6 eV), as well as higher integrated current density, to suggest lower rates of non-radiative recombination and fewer optical losses in devices based on SAMs than PTAA,^[11–13] which can be attributed to better charge extraction enabled by the ultrathin HTL.^[11]



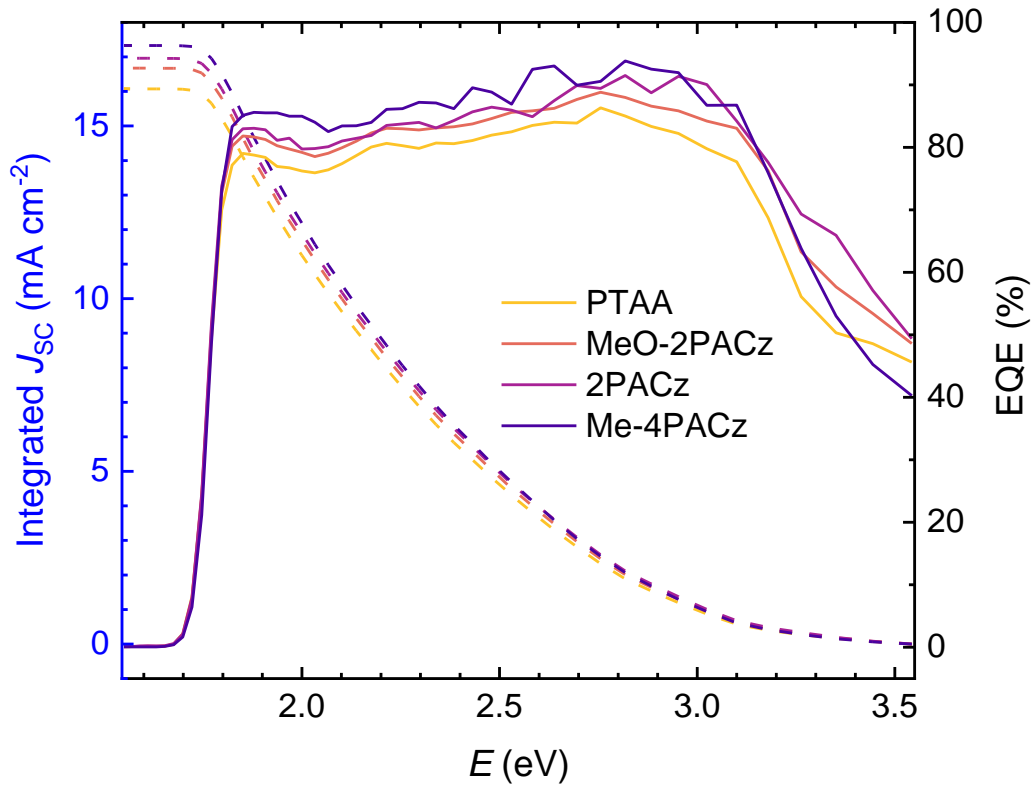
Supplementary Figure 1. (a) η_{mpp} , (b) steady-state V_{oc} , (c) steady-state J_{sc} and (d) quasi-FF of FA_{0.83}Cs_{0.17}Pb(I_{0.6}Br_{0.4})₃ PSCs employing PTAA, MeO-2PACz, 2PACz and Me-4PACz respectively as the hole transport layer. These devices were fabricated in a single experimental batch. Any pixel with $\eta_{\text{mpp}} \leq 75\% \eta_{\text{mpp}}$ of the champion device is cut off from the figure.



Supplementary Figure 2. *J-V* scan of the champion cells of $\text{FA}_{0.83}\text{Cs}_{0.17}\text{Pb}(\text{I}_{0.6}\text{Br}_{0.4})_3$ on PTAA, MeO-2PACz, 2PACz or Me-4PACz. Solid curve: reverse scan, dashed curve: forward scan. All performance metrics are given in **Supplementary Table 1**.

Devices	Scan Direction	V_{oc} (V)	J_{sc} /Integrated	FF	PCE (%)
			J_{sc}^* (mA cm ⁻²)		
PTAA	Reverse	1.09	16.4	0.72	12.7
	Forward	1.08	16.3	0.69	12.1
	Steady-State	1.08	15.8/16.1*	0.75	12.7
MeO-2PACz	Reverse	1.15	17.2	0.76	14.9
	Forward	1.13	17.1	0.74	14.2
	Steady-State	1.13	15.6/16.7*	0.79	14.0
2PACz	Reverse	1.22	16.9	0.74	15.3
	Forward	1.20	16.8	0.73	14.6
	Steady-State	1.21	16.8/17.0*	0.75	15.2
Me-4PACz	Reverse	1.22	17.3	0.76	16.1
	Forward	1.20	17.2	0.76	15.7
	Steady-State	1.22	17.1/17.3*	0.77	16.0

Supplementary Table 1. PV metrics of the champion cells of FA_{0.83}CS_{0.17}Pb(I_{0.6}Br_{0.4})₃ on PTAA, MeO-2PACz, 2PACz or Me-4PACz extracted from *J-V* scans in **Supplementary Figure 2**. *Integrated J_{sc} extracted from EQE measurements in **Supplementary Figure 3**.



Supplementary Figure 3. External quantum efficiency (EQE) spectra (right axis) and the corresponding integrated current density (integration of the product of EQE and AM 1.5G spectrum) (left axis) of the $\text{FA}_{0.83}\text{Cs}_{0.17}\text{Pb}(\text{I}_{0.6}\text{Br}_{0.4})_3$ perovskite solar cells based on PTAA, MeO-2PACz, 2PACz and Me-4PACz.

Supplementary Note 2

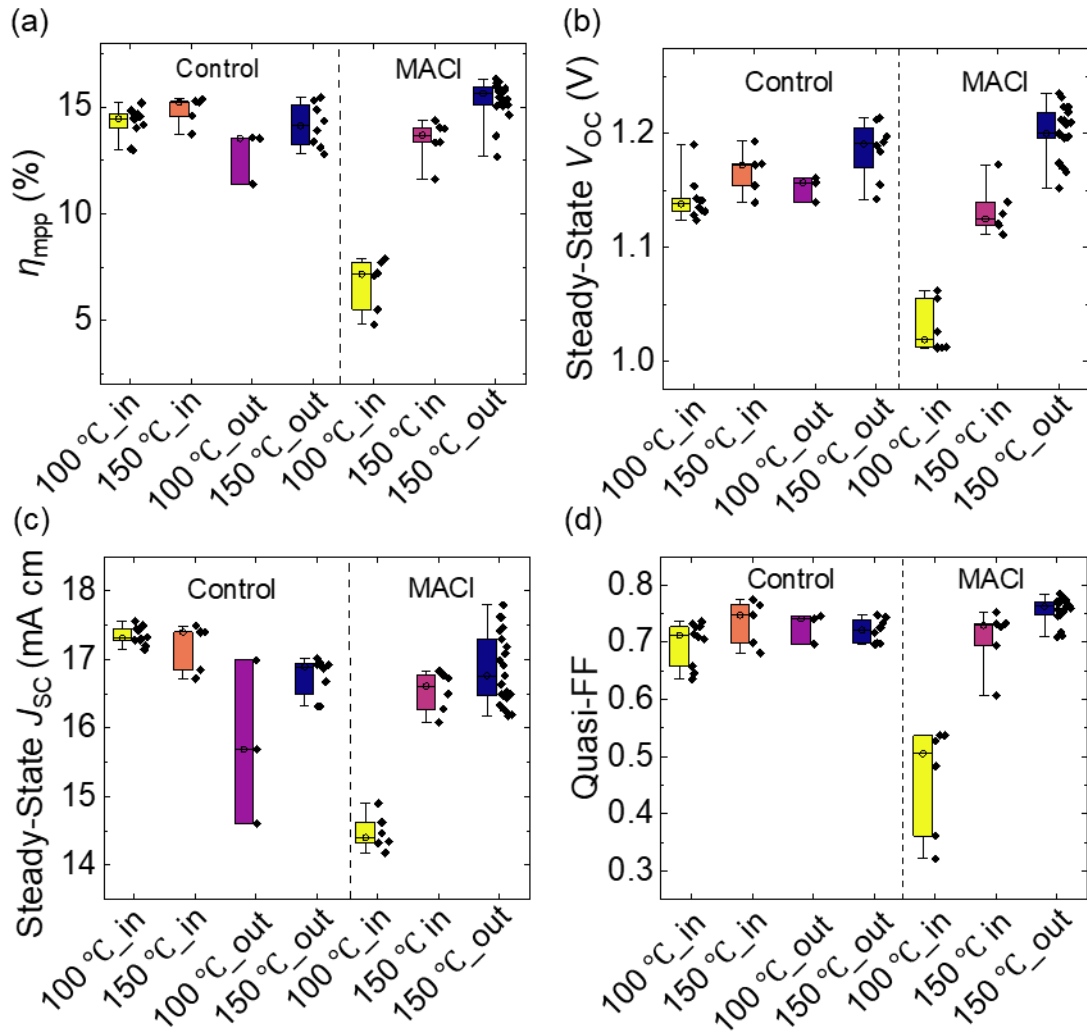
As mentioned in previous literature,^[14] methylammonium chloride (MACl) has been used as a crystallisation aid to improve the film quality and enlarge the grain size of triple-A-cation (FACsMA) perovskite films. In this work, we added an extra amount of MACl into a more complex perovskite composition ($\text{FA}_{0.83}\text{Cs}_{0.17}\text{Pb}(\text{I}_{0.6}\text{Br}_{0.4})_3$) and optimized the fabrication process of perovskite films (composition, annealing temperature and atmosphere). The involvement of high bromide contents in the precursor will change the crystallisation dynamics of perovskite films,^[2] which is not elucidated yet.

Supplementary Figure 4 presents the PV parameters achieved by the MACl-free and MACl-doped $\text{FA}_{0.83}\text{Cs}_{0.17}\text{Pb}(\text{I}_{0.6}\text{Br}_{0.4})_3$ PSCs which were processed at various annealing conditions. A higher annealing temperature (150 °C) only slightly increased the V_{OC} in the absence of MACl additives, whereas substantial improvements in all the PV parameters could be realised with the aid of MACl. As mentioned in previous literature,^[1] MACl allowed a higher annealing temperature and improved the perovskite crystallinity. This is consistent with our XRD results (see **Supplementary Figure 8**). Interestingly, annealing at ambient environment (30% RH in air) in the presence of MACl led to further boost in the PV parameters compared to annealing in a N_2 -filled glovebox.

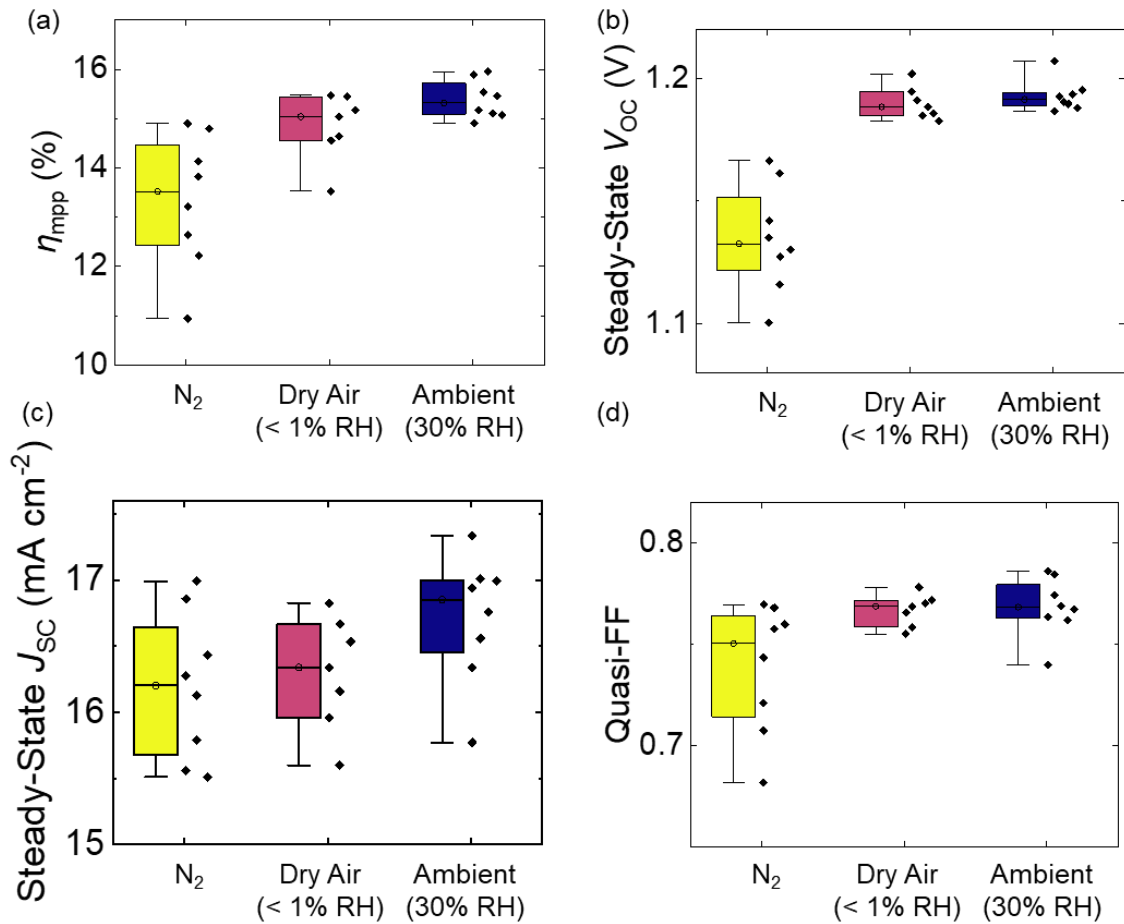
In order to decouple which factor accounted for the performance enhancement, we conducted further investigations. As shown in **Supplementary Figure 5**, by transferring the MACl-doped $\text{FA}_{0.83}\text{Cs}_{0.17}\text{Pb}(\text{I}_{0.6}\text{Br}_{0.4})_3$ films out of the glovebox after deposition and annealing the films in a compressed air-filled dry box (RH < 1%), the PV parameters (especially the V_{OC}) of the devices were improved compared to the films annealed in a N_2 -filled dry box (RH < 1%). Interestingly, annealing the MACl-modified perovskites at ambient condition with RH = 30% did not reduce the device performance, instead slightly higher FF and J_{SC} were achieved. We also demonstrate that the process performs comparably at a higher humidity level of 45% (**Supplementary Figure 6**). This suggests that there is a minimum humidity condition for optimal performance, but that there exists a wide processing window in which such performance can be achieved. However, for the best reproducibility of the process, we employed a controlled RH level (30%) in further experiments. In a previous work

reported by Brenes et al.,^[15] the humid air treatment on MAPbI₃ perovskite films has been shown to enhance the photoluminescence (PL) intensity and lifetime, which resulted in reduced V_{oc} loss and improved J_{sc} and PCE of PSC devices, due to elimination of shallow surface states and minimal non-radiative losses. Therefore, the performance boost in our optimised MACl-based cells can be attributed to such a humid air-activated passivation effect as similar improvements in the optoelectronic properties of our MACl-modified films were observed (**Supplementary Figure 7**). Additionally, the time taken (50 - 60 s) to transfer the as-deposited films to the dry box for annealing was nearly the same in each scenario, hence, delayed annealing did not contribute critically to the enhanced performance.

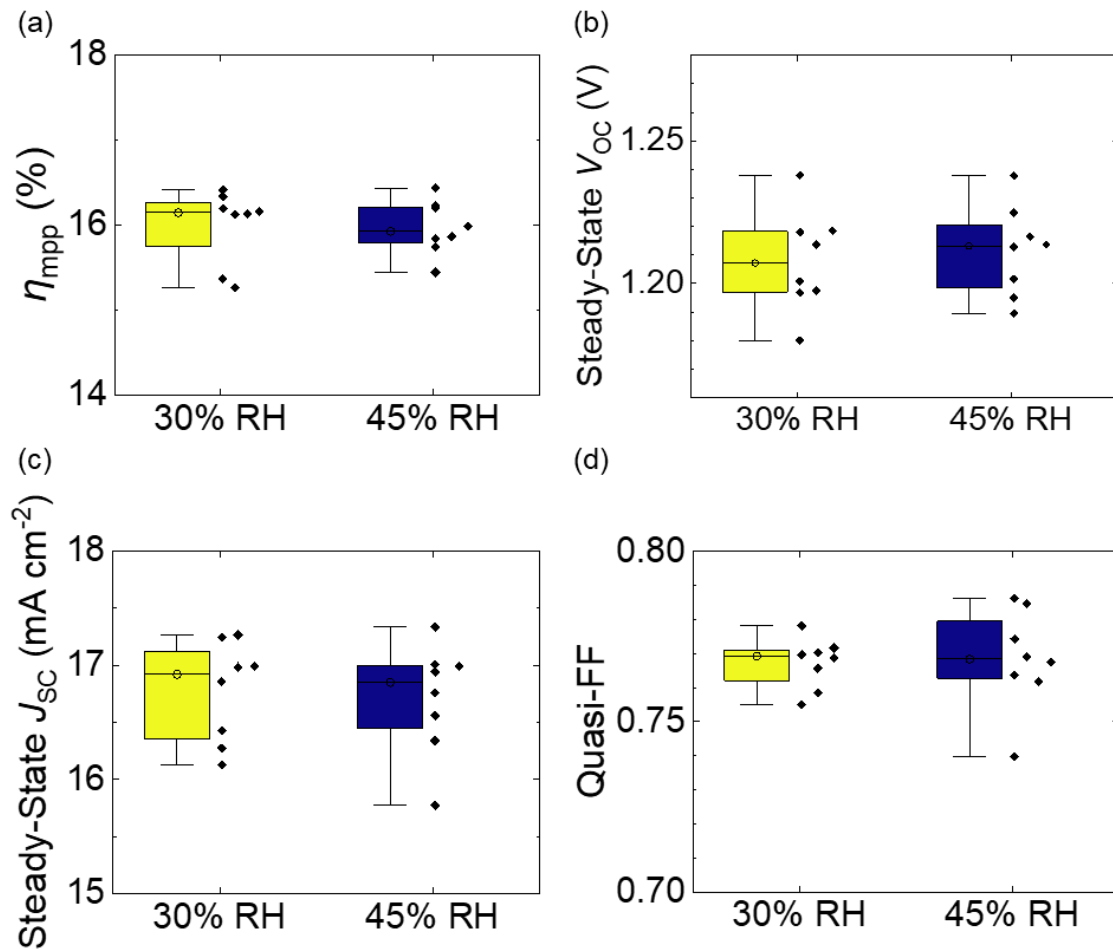
Out of the scope of this paper, we also examined another 1.8 eV perovskite composition FA_{0.75}Cs_{0.25}Pb(I_{0.7}Br_{0.3}) (with 10 mol% excess MAPbCl₃ additive, Cs₂₅Br₃₀+Cl₁₀) reported in previous literature,^[1] which employed 10 mol% excess of MAPbCl₃ into a FA-Cs mixed halide perovskite to make the so-called 'triple halide' perovskite. We fabricated a range of PSCs with different hole transport layers including PTAA, Poly-TPD and Me-4PACz. Based on our initial results (**Supplementary Figure 34 and 35**), this composition showed much poorer PV metrics especially η_{mpp} , steady-state J_{sc} and quasi-FF compared to our optimised composition (FA_{0.83}Cs_{0.17}Pb(I_{0.6}Br_{0.4})₃ with 15 mol% MACl additive). Even in the J - V scan of the champion cell based on Me-4PACz (**Supplementary Figure 35**), the Cs₂₅Br₃₀+Cl₁₀ cells suffer from severe hysteresis which is undesirable in p-i-n devices, therefore, we carried out our further investigation on FA_{0.83}Cs_{0.17}Pb(I_{0.6}Br_{0.4})₃ with 15 mol% MACl additive.



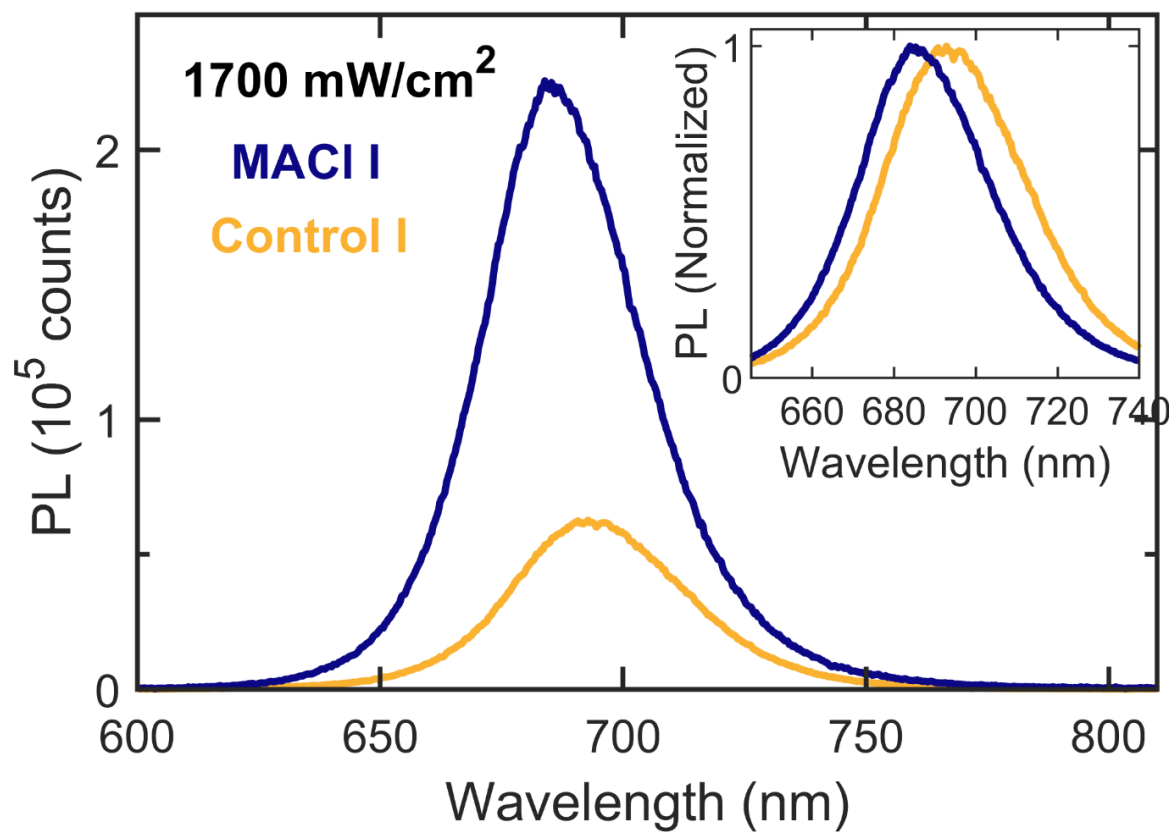
Supplementary Figure 4. PV parameters of $\text{FA}_{0.83}\text{Cs}_{0.17}\text{Pb}(\text{I}_{0.6}\text{Br}_{0.4})_3$ PSCs based on Me-4PACz with no MACI additives (control) or 15 mol% MACI additives annealed at different conditions: (a) η_{mpp} , (b) steady-state V_{OC} , (c) steady-state J_{sc} , (d) quasi-FF. The devices were either annealed in the glovebox (N_2 atmosphere, 'in') or transferred out of the glovebox immediately after deposition and annealed at ambient conditions (RH = 30%, 'out'). The annealing temperature and time were selected between 30 min at 100 °C ('100C') or 10 min at 150 °C ('150C'). All devices (59 cells) were fabricated in two batches of experiments.



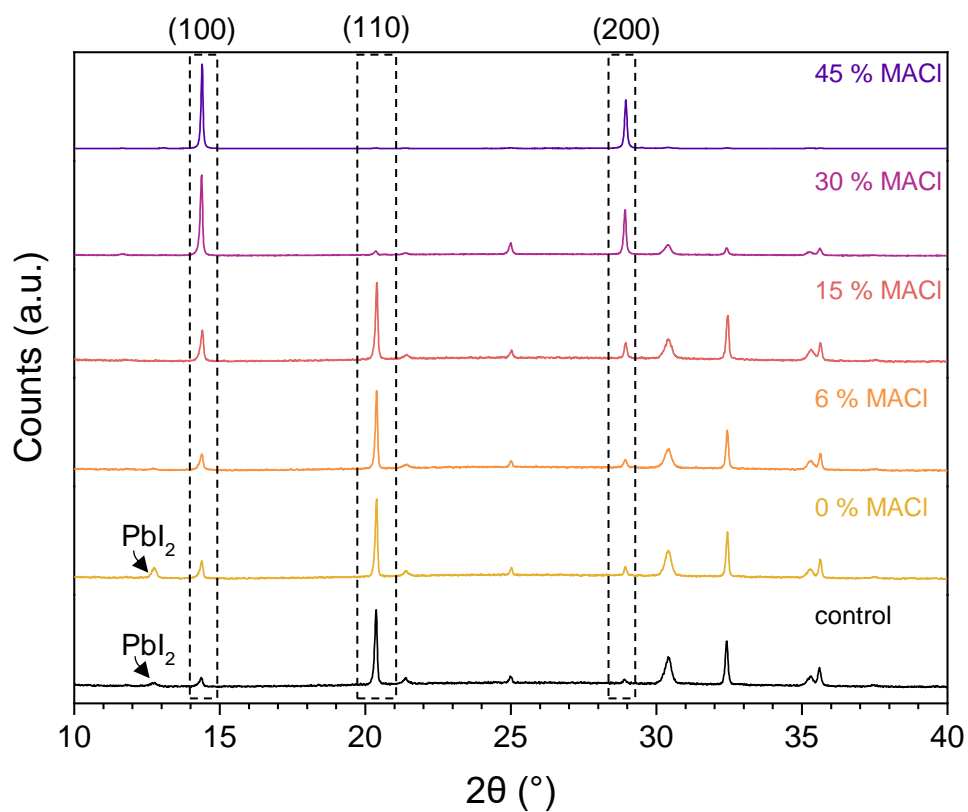
Supplementary Figure 5. PV parameters of FA_{0.83}Cs_{0.17}Pb(I_{0.6}Br_{0.4})₃ PSCs based on Me-4PACz with 15 mol% MACl additives annealed at various conditions: (a) η_{mpp} , (b) steady-state V_{oc} , (c) steady-state J_{sc} , (d) quasi-FF. The devices were deposited in the glovebox and transferred out to anneal at 150 °C for 10 min in a dry box purged with N₂ (< 1% RH, 'N₂'); or a dry box purged with compressed air (< 1% RH, 'Dry Air (< 1% RH)'); or at ambient conditions (30% RH, 'Ambient (30% RH)'). All devices (23 cells) were fabricated in one experimental batch.



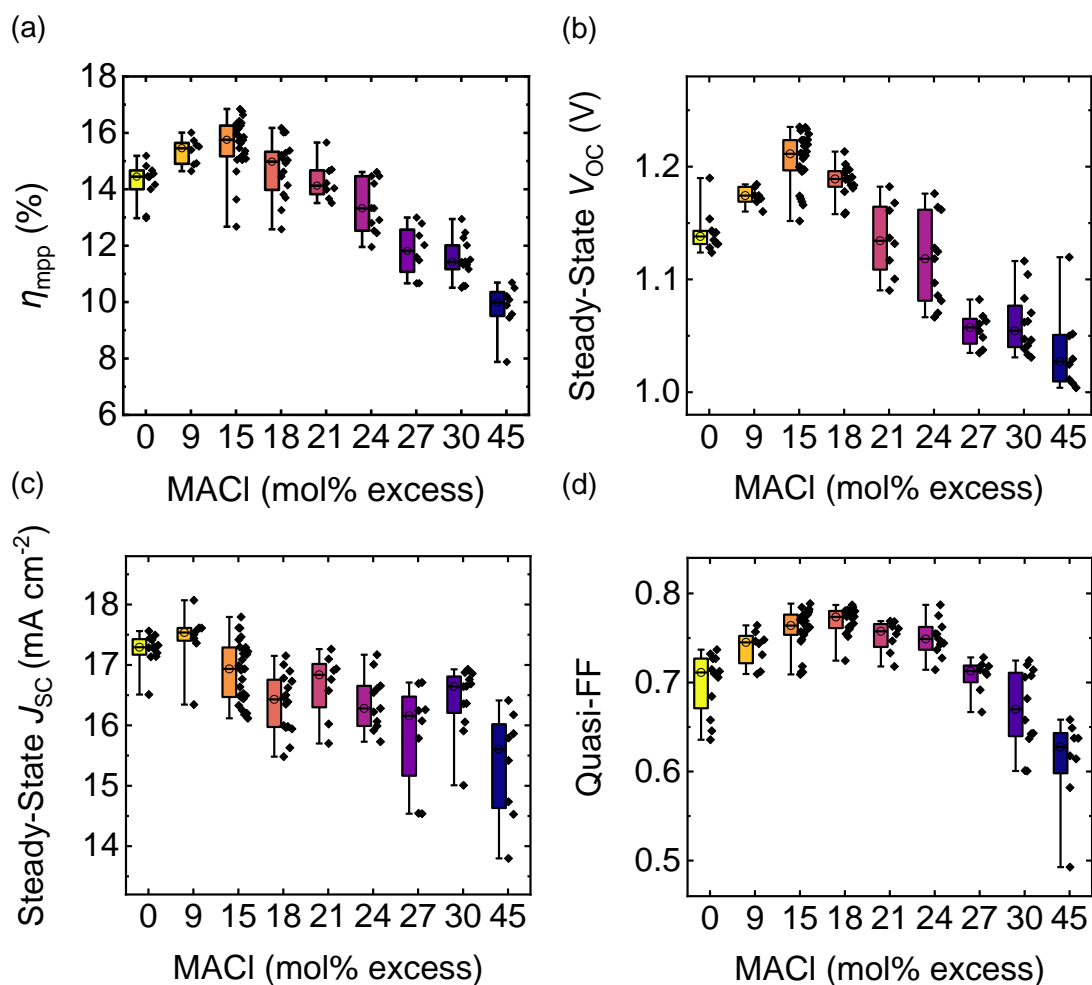
Supplementary Figure 6. PV parameters of $\text{FA}_{0.83}\text{Cs}_{0.17}\text{Pb}(\text{I}_{0.6}\text{Br}_{0.4})_3$ PSCs based on Me-4PACz with 15 mol% MACl additives annealed at different relative humidity (RH): (a) Maximum power point-tracked power conversion efficiency, η_{mpp} , (b) steady-state V_{oc} , (c) steady-state J_{sc} , (d) quasi-FF. The PSCs were deposited in an N_2 glovebox before being transferred out to anneal at 150 °C for 10 min in air controlled with different RH. (30% RH or 45% RH). All devices (16 cells) were fabricated in one experimental batch.



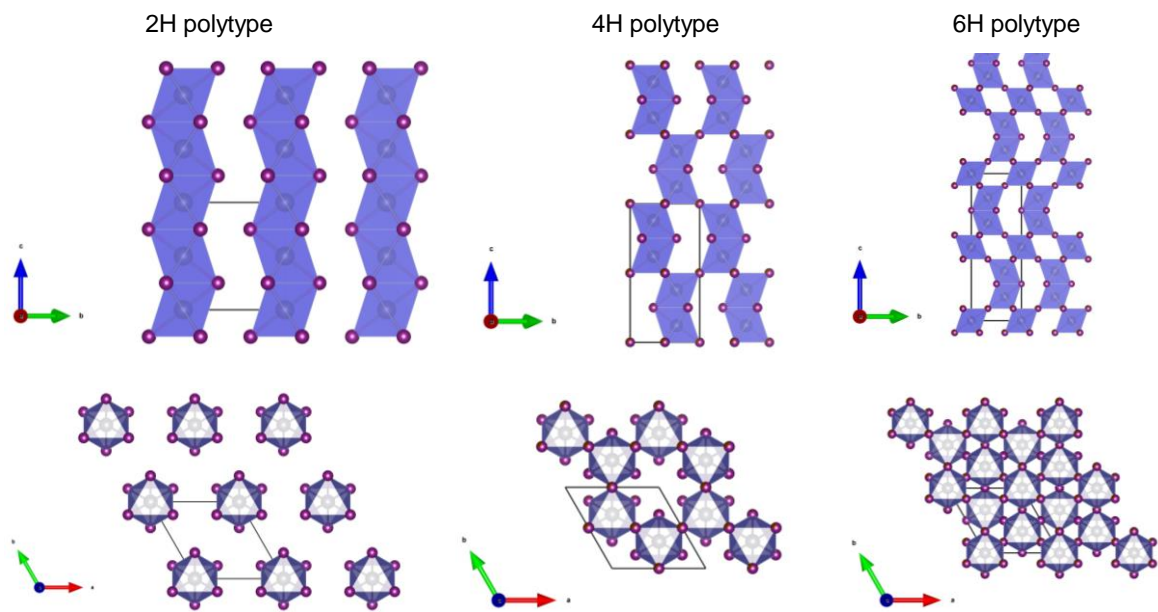
Supplementary Figure 7. Steady-state PL spectra of $\text{FA}_{0.83}\text{Cs}_{0.17}\text{Pb}(\text{I}_{0.6}\text{Br}_{0.4})_3$ perovskite films on quartz with or without 15 mol% MACl additive, namely 'MACl I' or 'Control I', under continuous illumination equivalent to 29 suns. Excitation wavelength is 398 nm. Inset: normalised PL spectra.



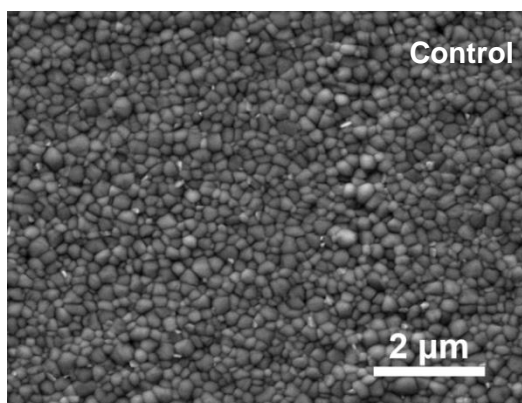
Supplementary Figure 8. X-ray diffraction (XRD) patterns of $\text{FA}_{0.83}\text{Cs}_{0.17}\text{Pb}(\text{I}_{0.6}\text{Br}_{0.4})_3$ as a function of MACl additive concentrations. ‘Control’ contains 0 mol% MACl additive and is annealed at 100 °C in a N_2 -filled glovebox, whereas perovskites fabricated with MACl additive are annealed at 150 °C in air with ~30% RH. ‘0 mol% MACl’ refers to a film without MACl additive but is annealed at 150 °C in air with ~30% RH.



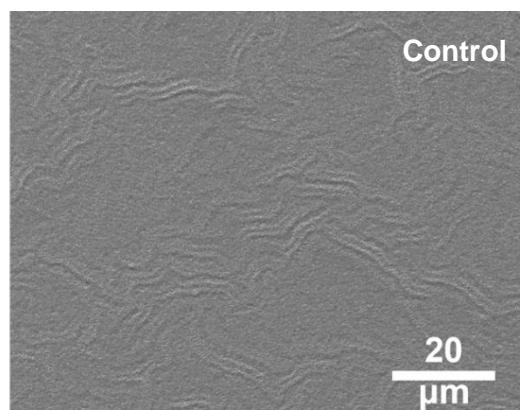
Supplementary Figure 9. PV parameters of $\text{FA}_{0.83}\text{Cs}_{0.17}\text{Pb}(\text{I}_{0.6}\text{Br}_{0.4})_3$ PSCs based on Me-4PACz with different excess molar ratio of MACI additives (0 - 45 mol%): (a) η_{mpp} , (b) steady-state V_{OC} , (c) steady-state J_{SC} , (d) quasi-FF. These devices (101 cells in total) were fabricated in 3 batches of experiments.



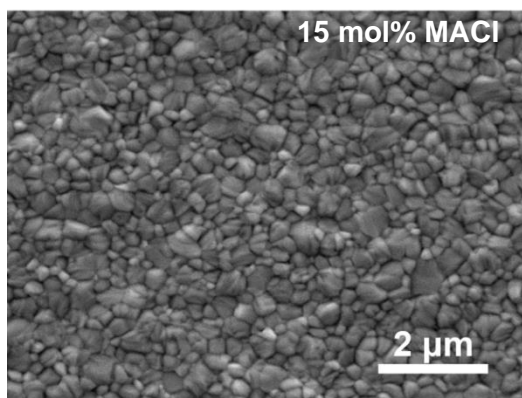
Supplementary Figure 10. Crystal diagrams of 2H, 4H and 6H polytypes.



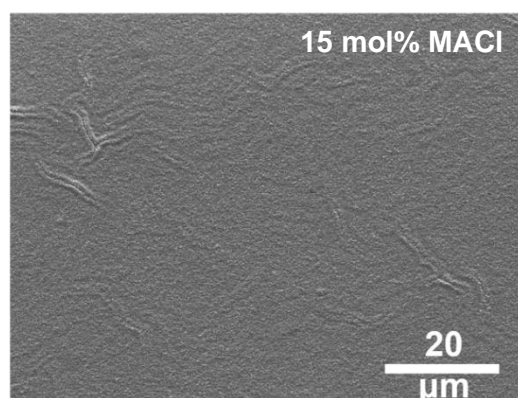
(a)



(b)

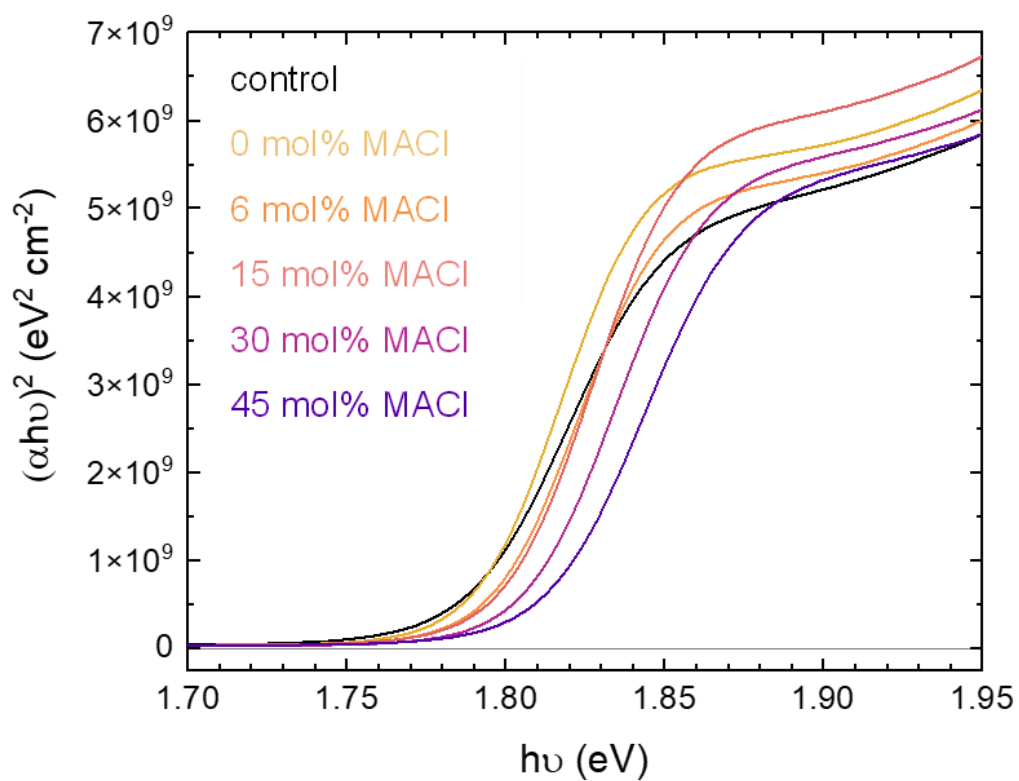


(c)

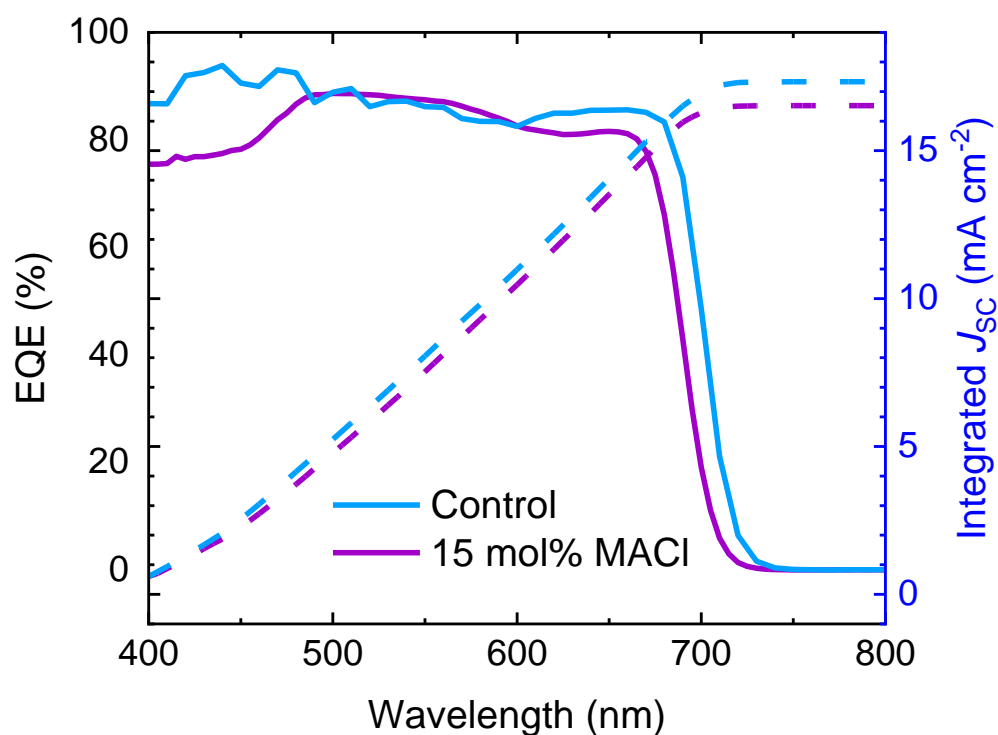


(d)

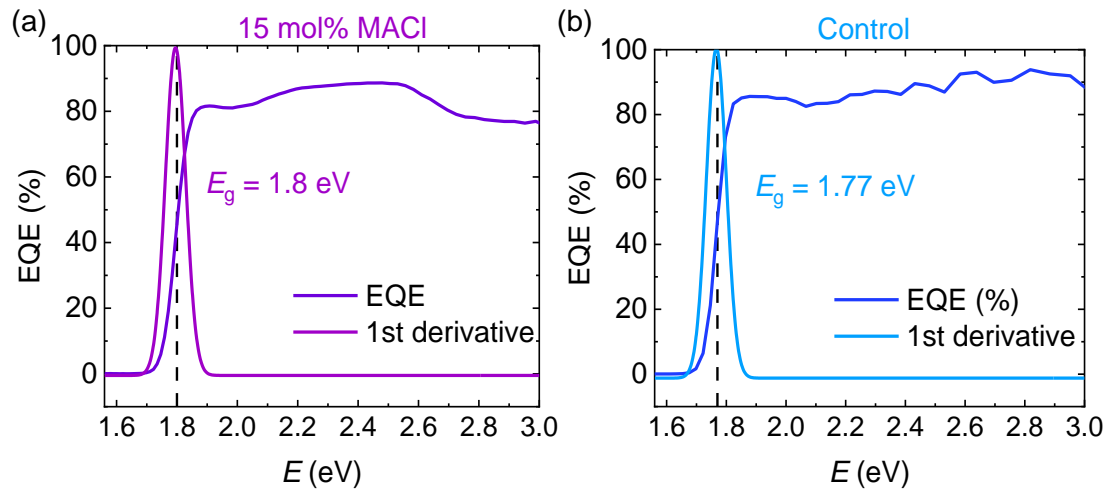
Supplementary Figure 11. Top-down SEM images of $\text{FA}_{0.83}\text{Cs}_{0.17}\text{Pb}(\text{I}_{0.6}\text{Br}_{0.4})_3$ films (a - b) without or (c - d) with 15 mol% MACl additive, namely 'Control' or '15mol% MACl'.



Supplementary Figure 12. Tauc analyses based on transmittance and reflectance measurements taken on $\text{FA}_{0.83}\text{Cs}_{0.17}\text{Pb}(\text{I}_{0.6}\text{Br}_{0.4})_3$ perovskites with a range of MACI concentrations (x) with $0 \leq x \leq 45$ mol%. “Control” contains 0 mol% MACI additive and is annealed at 100 °C in a N_2 glovebox. “0 mol% MACI” refers to a film without MACI additive but is annealed at 150 °C in air with ~30% RH.



Supplementary Figure 13. EQE and integrated J_{sc} for devices based on $\text{FA}_{0.83}\text{Cs}_{0.17}\text{Pb}(\text{I}_{0.6}\text{Br}_{0.4})_3$ with or without 15 mol% MACl additive, with Me-4PACz as the HTL and C_{60} as the ETL, namely '15 mol% MACl' or 'Control'.



Supplementary Figure 14. PV bandgap extracted from the inflection point of the onset of the EQE (**Supplementary Figure 13**) for devices based on $\text{FA}_{0.83}\text{Cs}_{0.17}\text{Pb}(\text{I}_{0.6}\text{Br}_{0.4})_3$ (a) with or (b) without 15 mol% MAI additive, with Me-4PACz as the HTL and C_{60} as the ETL, namely '15 mol% MAI' or 'Control'.

Supplementary Note 3

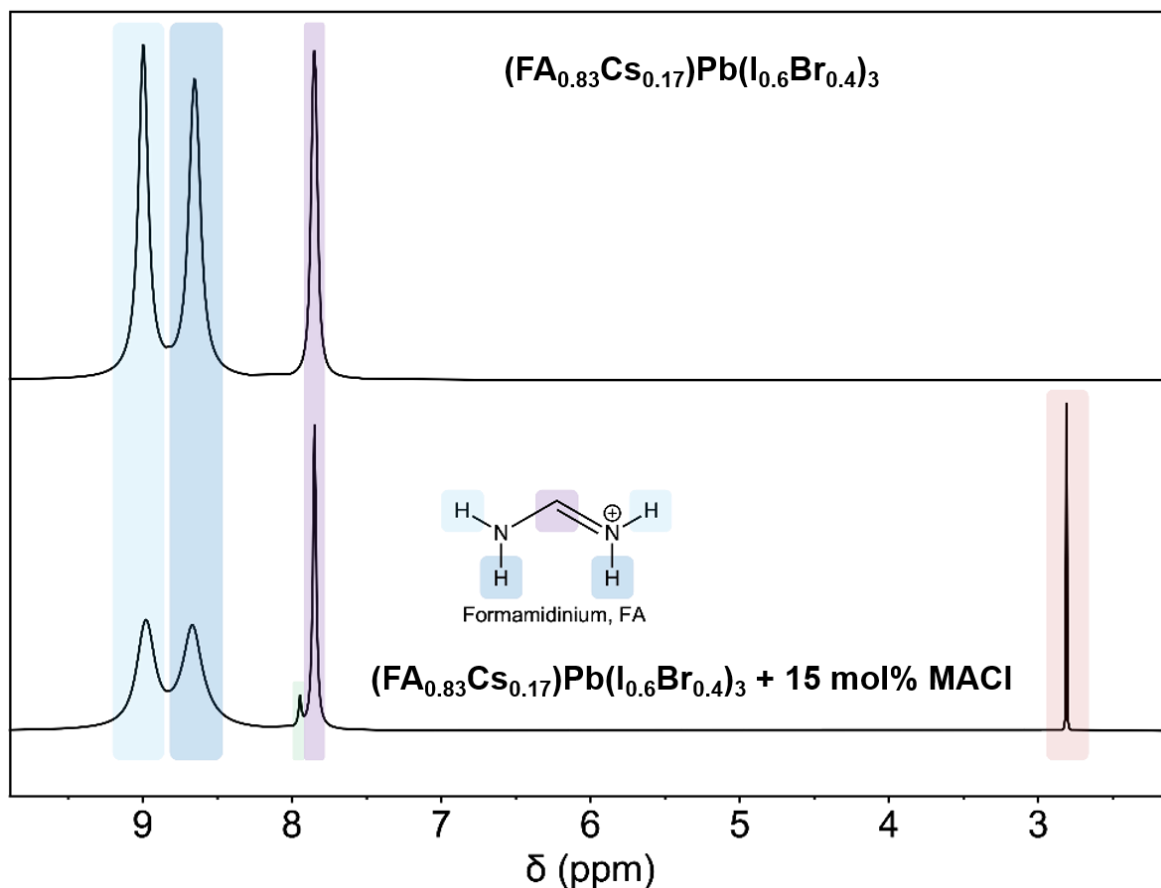
Supplementary Figure 15 shows ^1H liquid nuclear magnetic resonance (NMR) spectroscopy of our control and optimised (15 mol% MACl additive) perovskites. These spectra show signals corresponding to the ^1H environments of FA, along with two further signals in the case of the 15 mol% MACl material. This suggests the presence of a “non-FA” organic in this material. The chemical shift of these signals (7.95, 2.81 ppm) is such that they may correspond to MA, under which interpretation the signals are assigned as the ammonium (7.95 ppm) and methyl (2.81 ppm) ^1H environments. However, previous reports have shown the methyl ^1H nuclei of MA to have a chemical shift of <2.5 ppm,^[16] while signals corresponding to ammonium ^1H nuclei are typically not resolved due to exchange broadening (on account of the acidity of the ammonium group). We further note the similarity in the chemical shifts of these new signals and those reported previously for *N*-methyl formamidinium (MFA).^[17] However, as is typical of solutions containing coordinating ions, a selection of other reports have shown somewhat different chemical shifts corresponding to MFA,^[18,19] including resolution of its different structural isomers. In our experience (i) the concentration of the organic species in solution, (ii) the concentration of (in particular) halide ions, (iii) the identity of those halide ions, and (iv) the identity of the solvent used can all substantially affect the observed chemical shift of signals in liquid ^1H NMR spectra of perovskite materials. The concentration of organic species expected in solutions of dissolved perovskite thin films is relatively low; ca. 25 mg mL^{-1} of perovskite material, corresponding to an FA concentration of ca. 0.04 mM . Given this, acquisition of spectra other than 1D ^1H NMR with sufficient signal to noise to resolve resonance signals is non-trivial and beyond the scope of the current work. For example, acquisition of ^{13}C , ^1H - ^1H correlation and heteronuclear single quantum coherence spectroscopy are precluded for this reason. As such, we are not able to unambiguously identify whether this secondary organic species is methylammonium or another organic cation.

It is, however, important to confirm that inclusion of MA, MFA or any other organic species is not the cause of the observed bandgap increase. To do this we measure the absorbance and XRD of perovskite films fabricated with the addition of a range of AX additives at 15 mol% (**Supplementary Figures 16 & 17**). Here, additives were

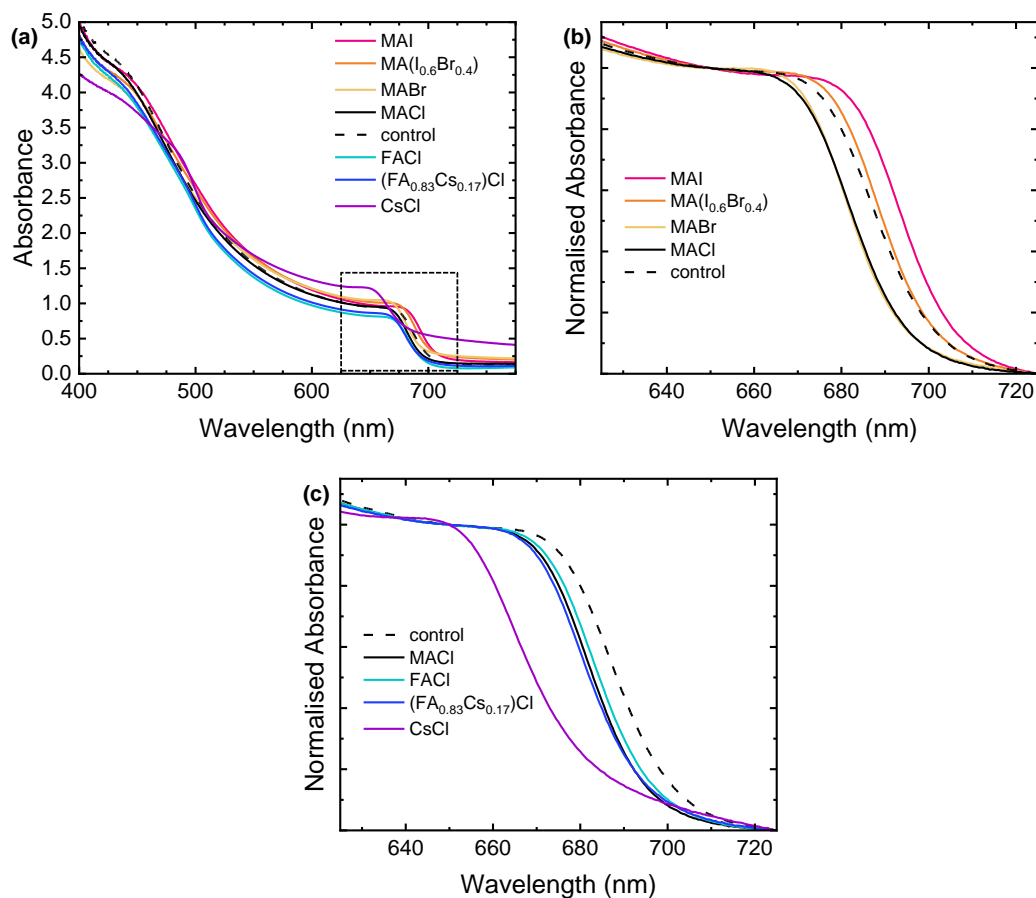
chosen so as to isolate certain cations or halides, so that we can infer the influence of each ion on the resultant perovskite optical bandgap.

Supplementary Figure 16b shows that MA(I_{0.6}Br_{0.4}) addition – in which the halide stoichiometry of the parent perovskite, FA_{0.83}Cs_{0.17}Pb(I_{0.6}Br_{0.4})₃, is preserved – has negligible influence on absorbance onset. We interpret this to indicate that any MA remaining in the final perovskite material after fabrication has negligible influence on the bandgap. This figure also reveals that the absorbance onset is blue-shifted by a similar energy if MABr or MACl additives are used. As chloride incorporated into the perovskite lattices is expected to produce a proportionally more significant onset than bromide, we deduce that less additive chloride than additive bromide remains in the fabricated perovskites despite the additive loading being equal (15 mol%). This suggests that either (i) chloride is less readily incorporated into the perovskite material than bromide, or (ii) incorporated chloride is more easily lost during post-deposition thermal curing.

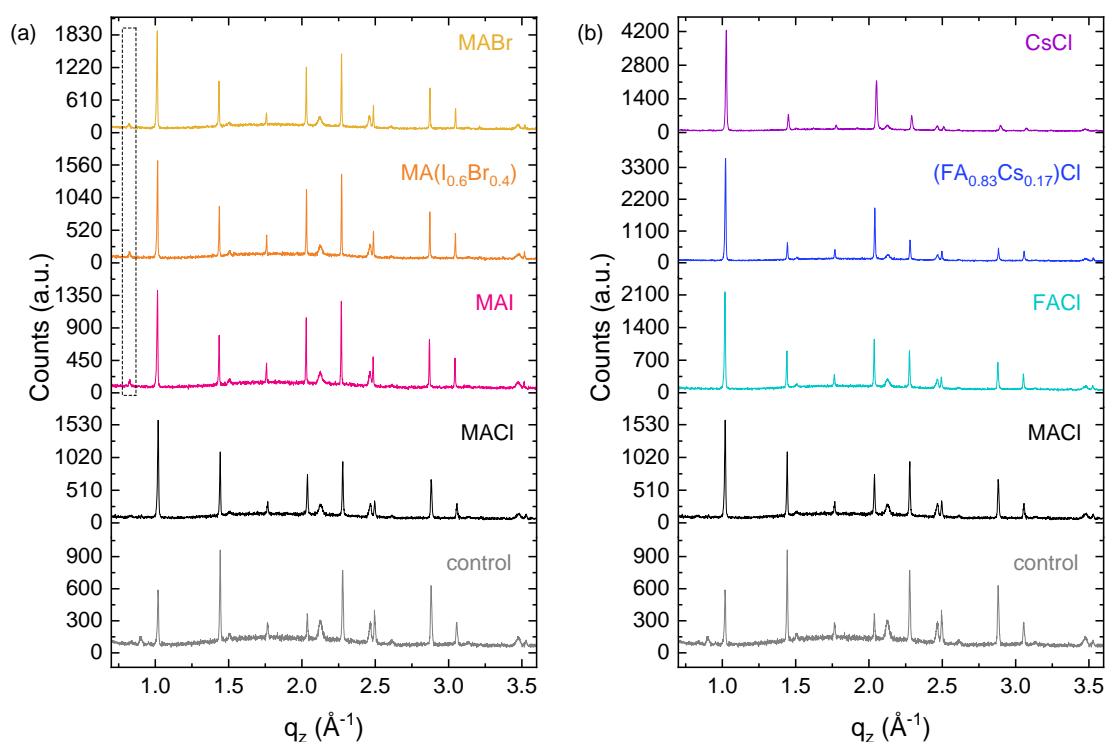
Supplementary Figure 16c shows that all ACI additives investigated lead to a blue-shifted absorbance onset. We find that addition of MACl and of (FA_{0.83}Cs_{0.17})Cl lead to very similar absorbance onsets, again suggesting that MA-incorporation yields negligible influence over the bandgap of FA_{0.83}Cs_{0.17}Pb(I_{0.6}Br_{0.4})₃. Notably, CsCl addition leads to a substantial blueshift in the absorbance onset. As Cs is known to widen the bandgap of FA-rich perovskites, this indicates that Cs is incorporated alongside Cl and is retained in the final perovskite after thermal curing. In light of these results, we attribute the observed increase in optical bandgap to the inclusion of Cl within the perovskite lattice. This also indicates that Cl-incorporation is not co-dependent on MA incorporation. We also confirm Cl-incorporation with Wavelength Dispersive X-Ray Fluorescence measurement in **Supplementary Note 4**.



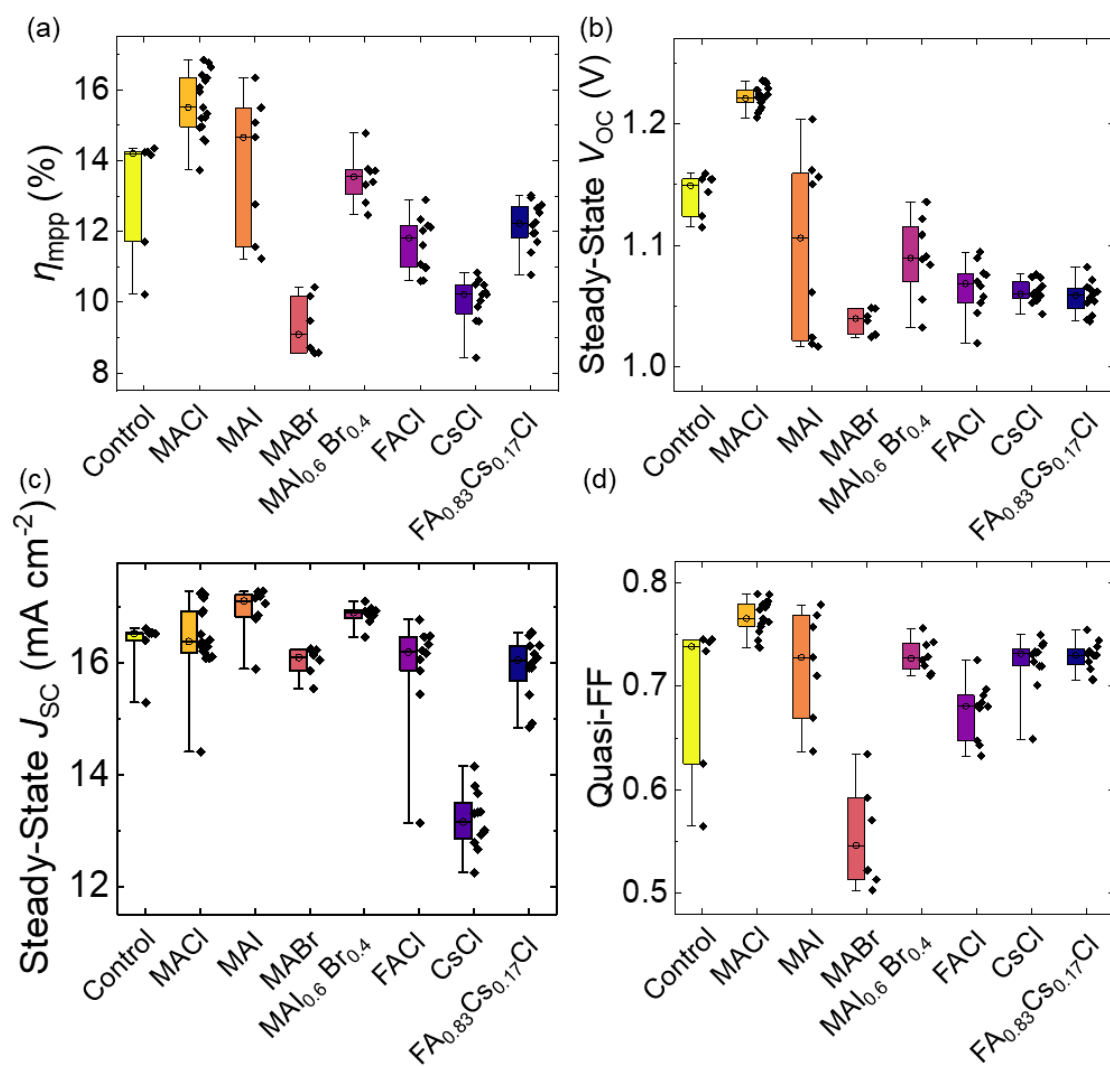
Supplementary Figure 15: ^1H liquid nuclear magnetic resonance (NMR) spectra of control (top) and optimised (15 mol% MACl additive, bottom) perovskite materials. Spectra are obtained by dissolving material from ca. 50 cm^2 of perovskite thin film material (ca. 450 nm thickness) in $\text{DMSO-}d_6$. Spectra are referenced to DMSO signal (not shown).



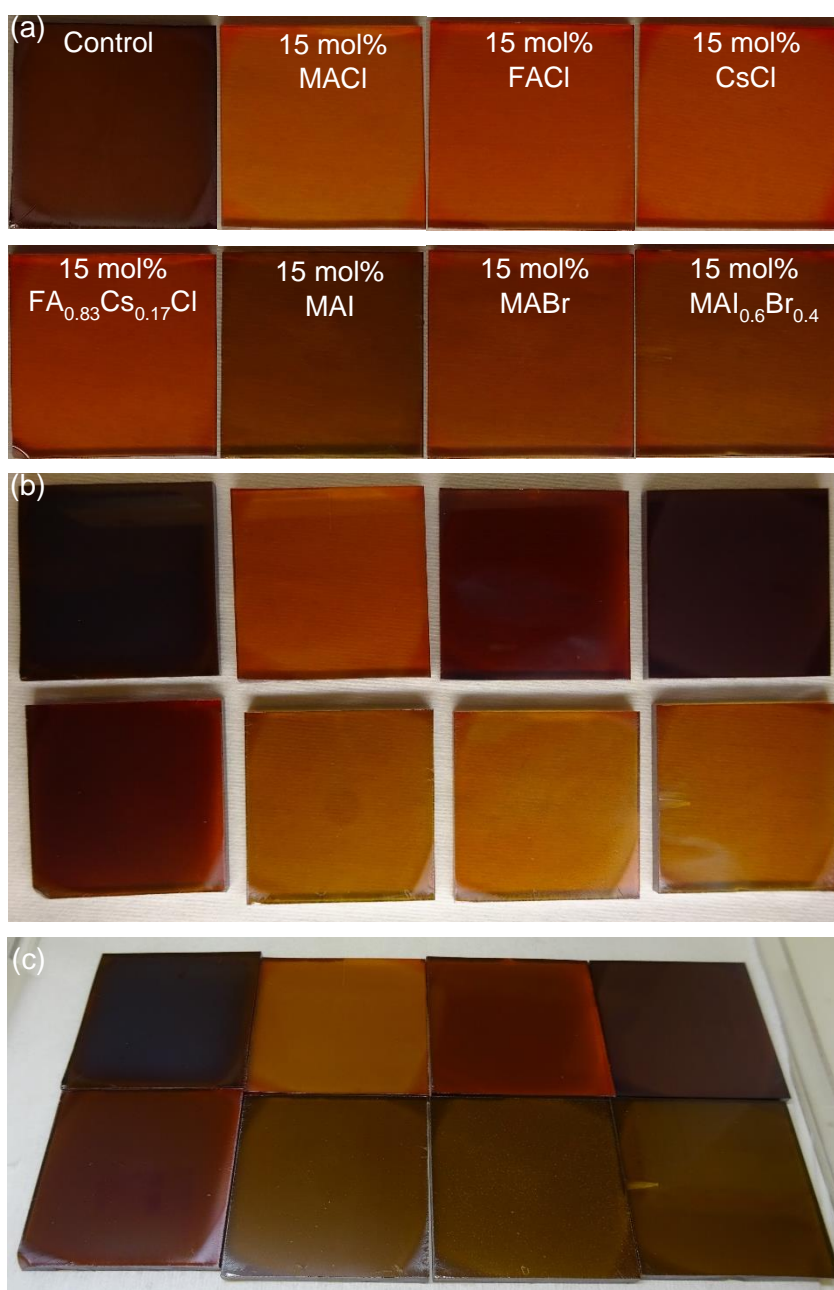
Supplementary Figure 16. (a) Absorbance spectra of a range of $\text{FA}_{0.83}\text{Cs}_{0.17}\text{Pb}(\text{I}_{0.6}\text{Br}_{0.4})_3$ perovskites each with 15 mol% additive A-site halide. $\text{MA}(\text{I}_{0.6}\text{Br}_{0.4})$ represents a mixed-halide additive with 0.6:0.4 MAI:MABr stoichiometry, at 15 mol% excess with respect to MA. $(\text{FA}_{0.83}\text{Cs}_{0.17})\text{Cl}$ represents a mixed-A-site additive 0.83:0.17 with FAcI:CsCl, at 15 mol% excess with respect to Cl. The region of the spectrum highlighted in the box is expanded and the absorbance spectra normalised between 650 and 725 nm to emphasise the bandgap shifts observed as a result of 15 mol% AX addition: (b) shows the influence of MAX additives, (c) shows the influence of ACl additives.



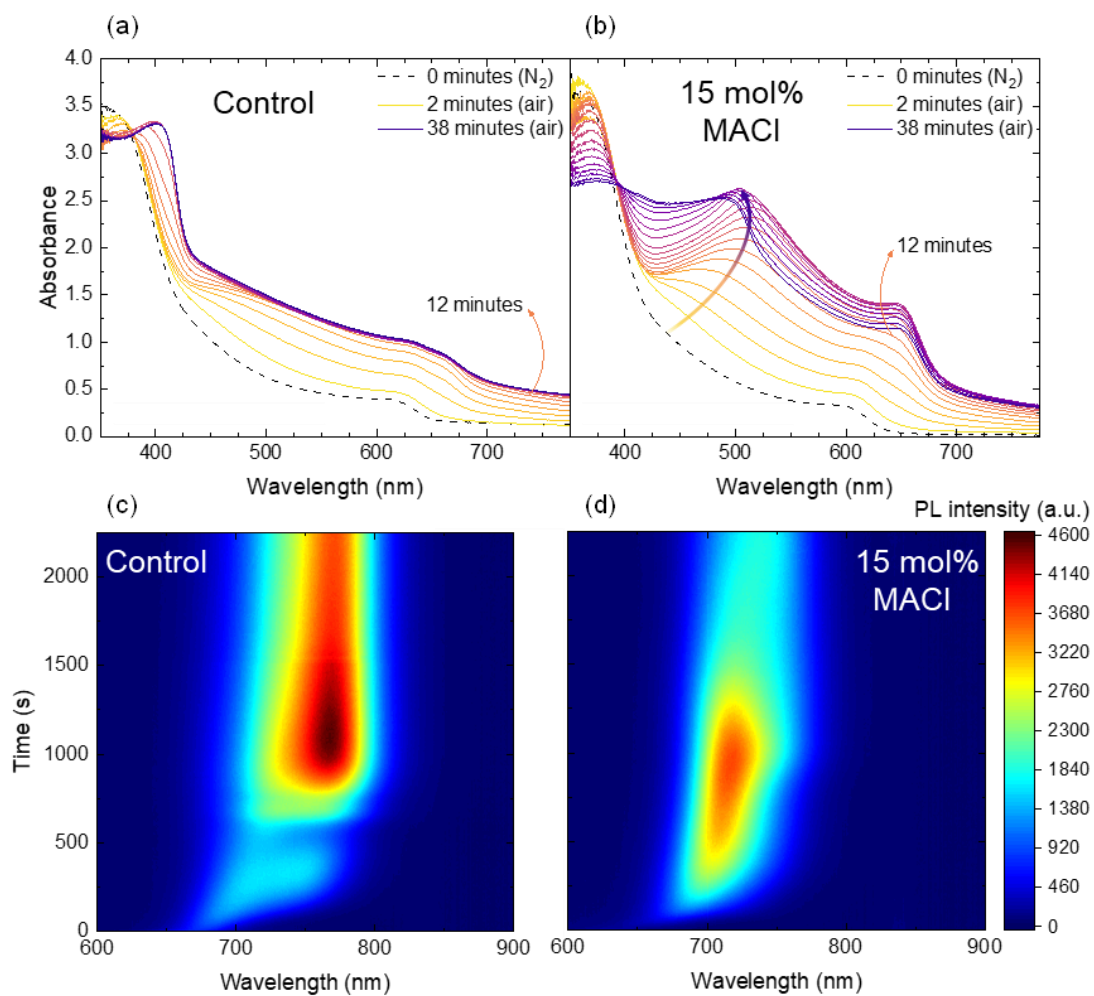
Supplementary Figure 17. X-ray diffraction patterns (XRD) showing the perovskite materials obtained by employing various AX-type additives at 15 mol% excess into $\text{FA}_{0.83}\text{Cs}_{0.17}\text{Pb}(\text{I}_{0.6}\text{Br}_{0.4})_3$. $\text{MA}(\text{I}_{0.6}\text{Br}_{0.4})$ represents a mixed-halide additive with 0.6:0.4 MAI:MABr stoichiometry, at 15 mol% excess with respect to MA. $(\text{FA}_{0.83}\text{Cs}_{0.17})\text{Cl}$ represents a mixed-A-site additive 0.83:0.17 with FACl:CsCl, at 15 mol% excess with respect to Cl. The region of highlighted with a box emphasises the formation of lower-dimensionality polytypes in the presence of MAI and MABr additives. The halide composition affected the lattice parameters as expected.



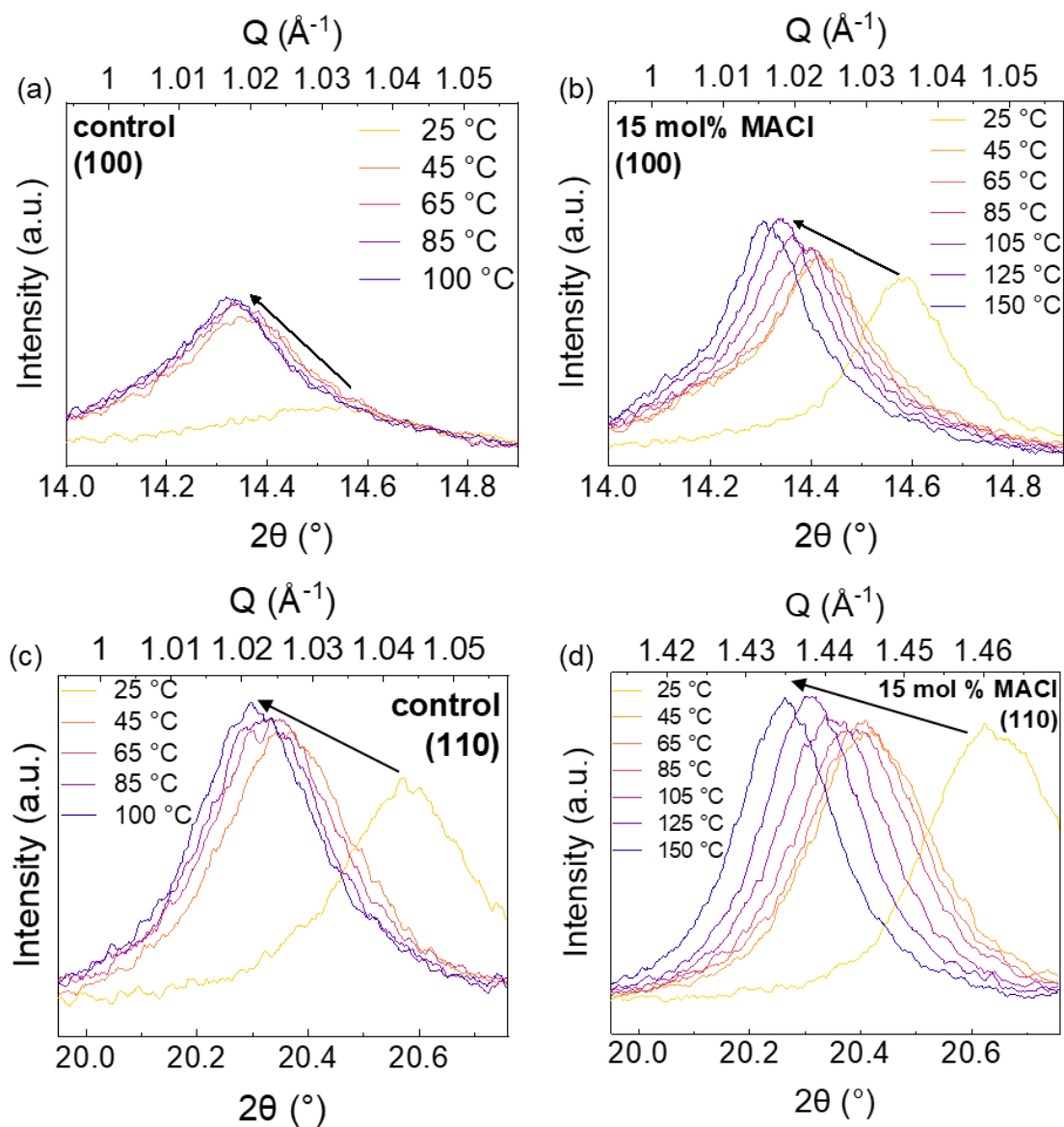
Supplementary Figure 18. Statistics of (a) η_{mpp} , (b) steady-state V_{oc} , (c) steady-state J_{sc} and (d) quasi-FF values of $\text{FA}_{0.83}\text{Cs}_{0.17}\text{Pb}(\text{I}_{0.6}\text{Br}_{0.4})_3$ devices based on Me-4PACz with no additive (control, 6 cells), or with 15 mol% addition of MACl (17 cells), %FAcI (7 cells), %CsCl (6 cells), % $\text{FA}_{0.83}\text{Cs}_{0.17}\text{Cl}$ (8 cells), %MAI (10 cells), %MABr (12 cells) or % $\text{MAI}_{0.6}\text{Br}_{0.4}$ (12 cells). These cells were fabricated across two batches of experiments.



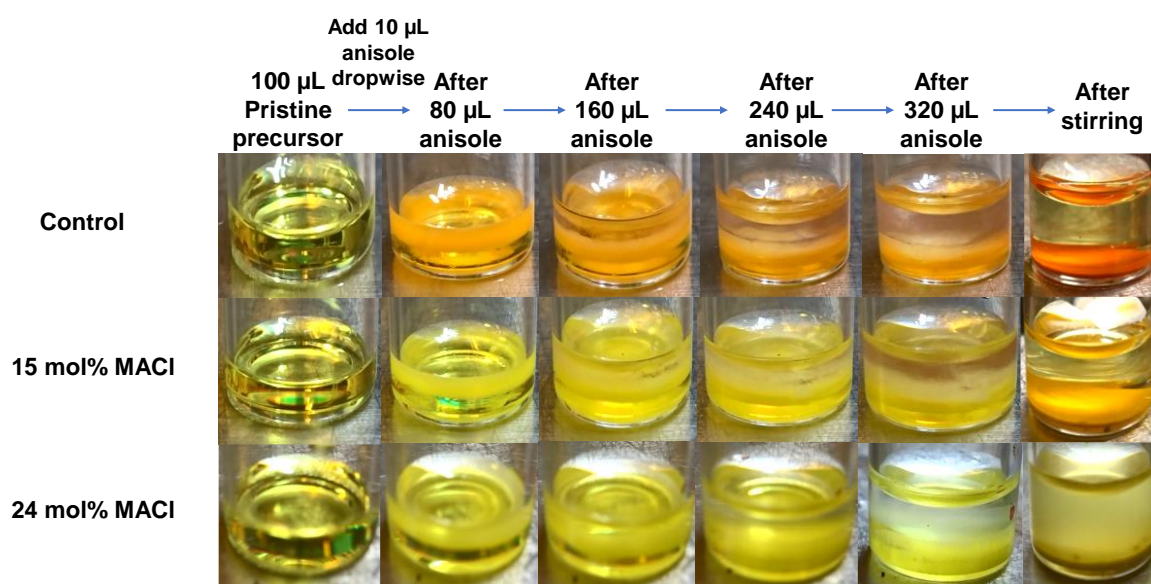
Supplementary Figure 19. Photos of the intermediate phases of $\text{FA}_{0.83}\text{Cs}_{0.17}\text{Pb}(\text{I}_{0.6}\text{Br}_{0.4})_3$ with no additive (Control) or with 15 mol% MACl, FAcI, CsCl, $\text{FA}_{0.83}\text{Cs}_{0.17}\text{Cl}$, MAI, MABr or $\text{MAI}_{0.6}\text{Br}_{0.4}$ taken (a) immediately after spin coating (b) 30 min stored under N_2 atmosphere and (c) 60 min stored under N_2 atmosphere followed by exposure to air for 5 min.



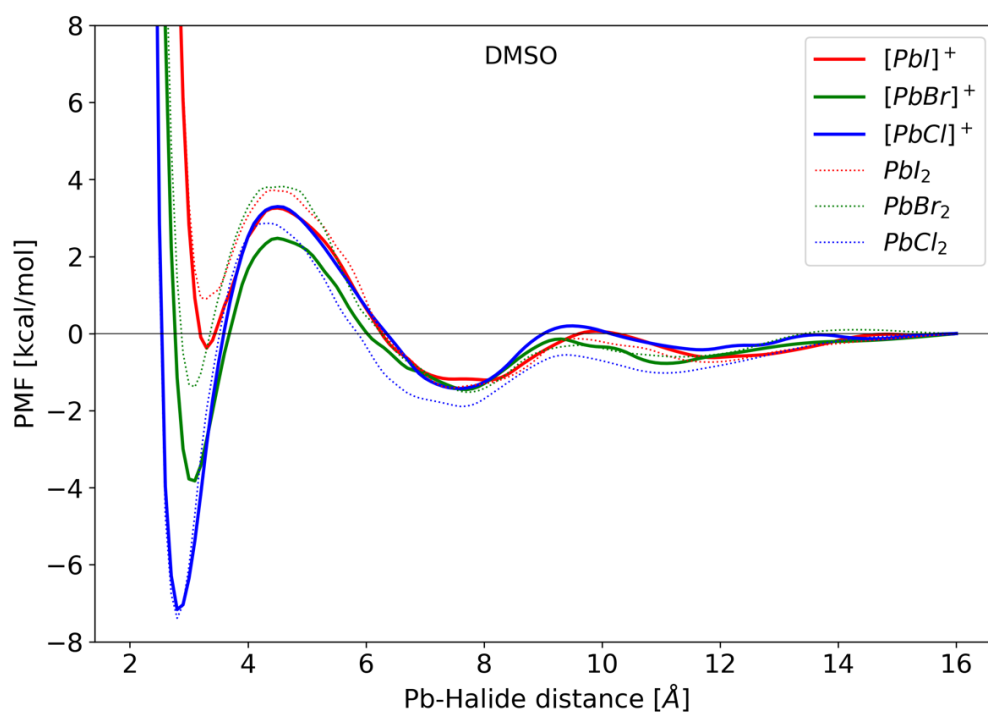
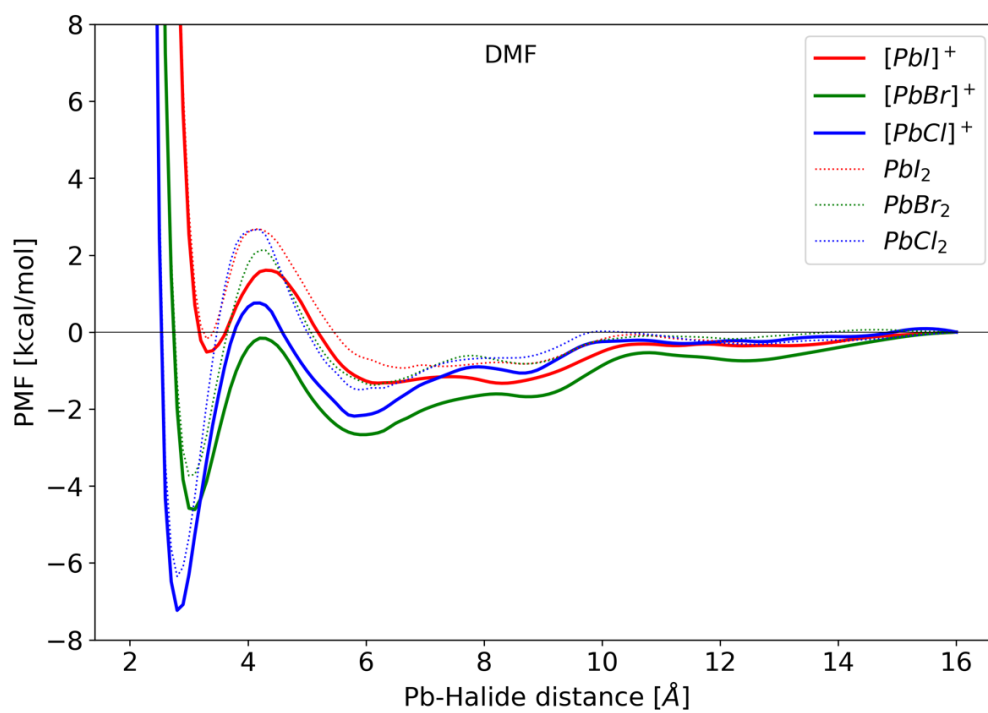
Supplementary Figure 20. Evolution of the absorption and photoluminescence spectra of the antisolvent-quenched (a & c) $\text{FA}_{0.83}\text{Cs}_{0.17}\text{Pb}(\text{I}_{0.6}\text{Br}_{0.4})_3$ films and (b & d) $\text{FA}_{0.83}\text{Cs}_{0.17}\text{Pb}(\text{I}_{0.6}\text{Br}_{0.4})_3$ with 15 mol% MACI measured under ambient conditions (25 °C, RH ~ 50% in air), namely 'Control' and '15 mol% MACI'.



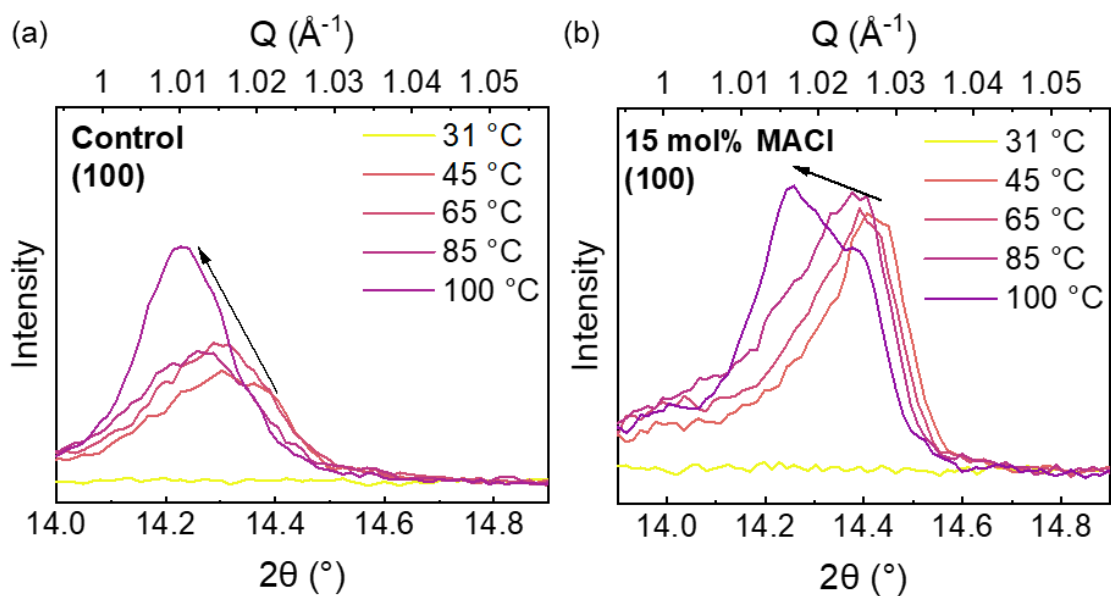
Supplementary Figure 21. XRD patterns tracking the evolution of cubic perovskite (100) and (110) reflections during step-wise annealing of $\text{FA}_{0.83}\text{Cs}_{0.17}\text{Pb}(\text{I}_{0.6}\text{Br}_{0.4})_3$ perovskite films (a - b) with or (c - d) without 15 mol% MACl additive, namely '15 mol% MACl' and 'control'. The temperature range for step-wise annealing is analogous to the device processing conditions (150 °C for MACl-processed film and 100 °C for control film).



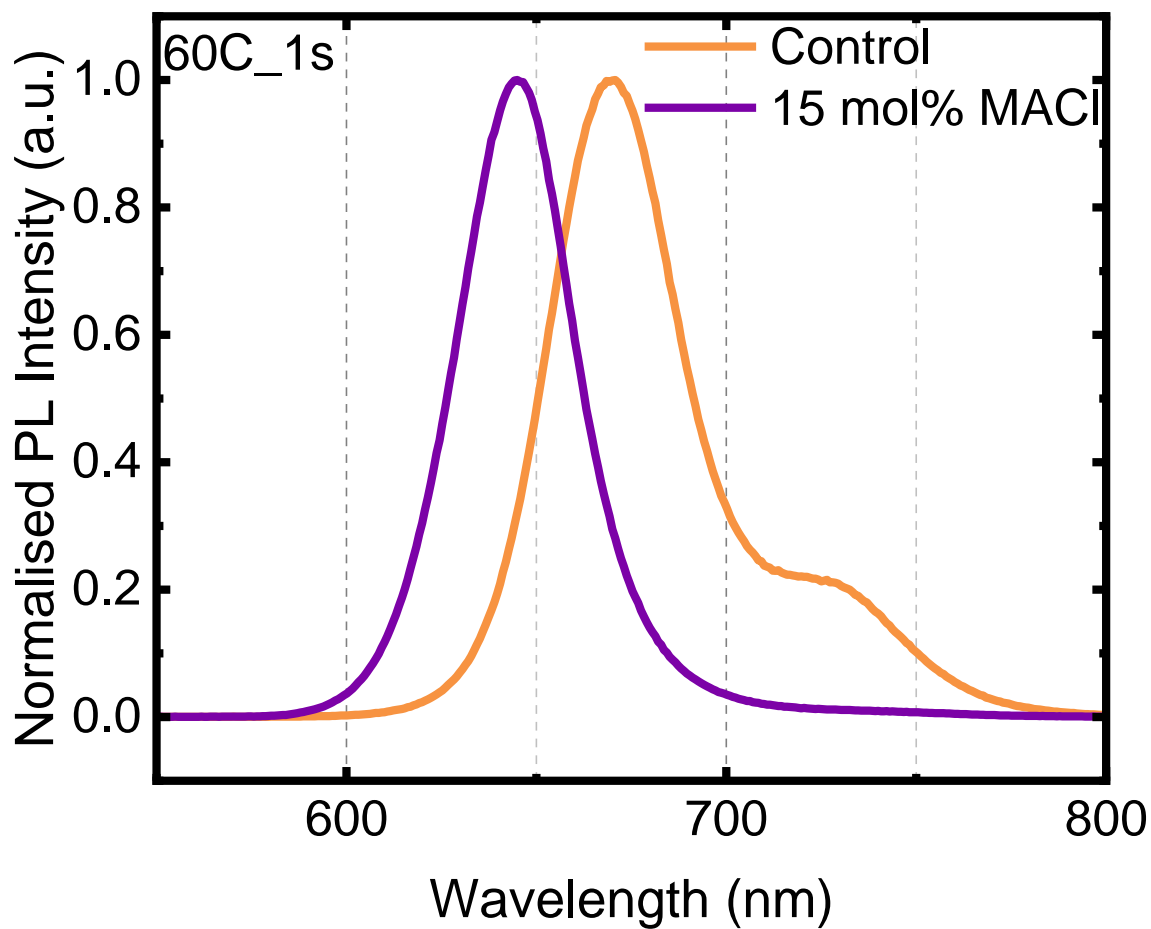
Supplementary Figure 22. Solvent quenching of the $\text{FA}_{0.83}\text{Cs}_{0.17}\text{Pb}(\text{I}_{0.6}\text{Br}_{0.4})_3$ without or with 15 mol% or with 24 mol% MACI additive, namely 'control', '15 mol% MACI' and '24 mol% MACI', perovskite precursor solutions under N_2 atmosphere by anti-solvent dripping with anisole. 320 μL of anisole is added dropwise (10 μL each time) into 100 μL of perovskite precursors. A same amount of anisole is used in our PSC device fabrications. Any changes in the solution appearance over time are recorded with a digital camera. The photos taken before antisolvent dripping; after adding 80 μL , 160 μL , 240 μL , 320 μL of anisole; stirring in glovebox after solvent quenching are shown in the graph.



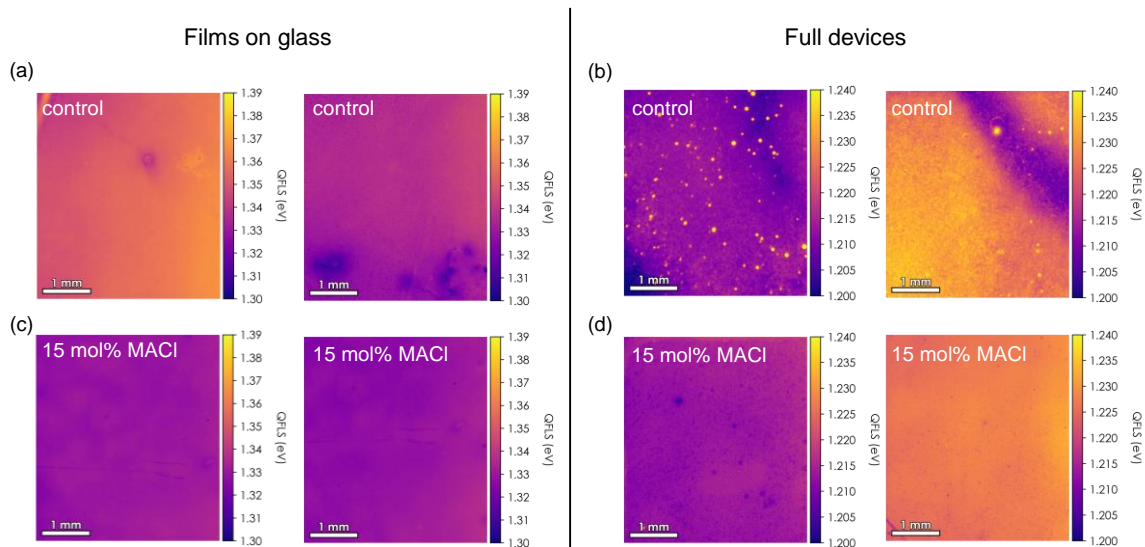
Supplementary Figure 23. Potentials of mean force (PMF) for the formation of [PbX]⁺ and PbX₂ complexes in DMF and in DMSO upon successive halide addition at 300 K.



Supplementary Figure 24. GIWAXS patterns tracking the evolution of cubic perovskite (100) reflection during step-wise annealing of $\text{FA}_{0.83}\text{Cs}_{0.17}\text{Pb}(\text{I}_{0.6}\text{Br}_{0.4})_3$ without or with 15 mol% MACl additive, namely 'control' or '15 mol% MACl'.



Supplementary Figure 25. Normalised PL spectra of intermediates formed for $\text{FA}_{0.83}\text{Cs}_{0.17}\text{Pb}(\text{I}_{0.6}\text{Br}_{0.4})_3$ and 15 mol% MAI-processed $\text{FA}_{0.83}\text{Cs}_{0.17}\text{Pb}(\text{I}_{0.6}\text{Br}_{0.4})_3$ after 1 seconds of thermal annealing at 60 °C, denoted as 'Control' and '15 mol% MAI'.



Supplementary Figure 26. Quasi-Fermi level splitting (QFLS) maps taken using an in house-built photoluminescence measurement setup on (a) thin films on glass (b) full devices of $\text{FA}_{0.83}\text{Cs}_{0.17}\text{Pb}(\text{I}_{0.6}\text{Br}_{0.4})_3$ perovskite compositions and (c) thin films on glass (d) full devices of $\text{FA}_{0.83}\text{Cs}_{0.17}\text{Pb}(\text{I}_{0.6}\text{Br}_{0.4})_3$ with 15 mol% MACI additive, namely 'control' and '15 mol% MACI'. Me-4PACz and C_{60} were used as HTL and ETL respectively in the full devices. Two films and two pixels were measured for each variable, small variations in the absolute QFLS values between different samples are shown in the graph. A 450 nm laser is used for photoexcitation.

Supplementary Note 4

In order to determine whether the MACl-modified perovskite retains Cl in the structure after processing, we carried out Wavelength Dispersive X-Ray Fluorescence (WDXRF) measurement on the $\text{FA}_{0.83}\text{Cs}_{0.17}\text{Pb}(\text{I}_{0.6}\text{Br}_{0.4})_3$ perovskite films with or without 15 mol% MACl and report the atomic percentages (at. %) of the halide and lead atoms in these materials (**Supplementary Table 2**). All samples were deposited on ITO substrates and the measured atomic percentage values have been corrected with a standard (blank ITO substrate). Two different samples were measured for each condition. In all the samples, the Pb to halide ratio and the iodide to bromide ratio are slightly shifted from the nominal stoichiometric ratio in the perovskite precursors (1:3 and 6:4 respectively). Similar observations have been reported in previous literature using XRF to quantify elemental distribution in perovskite films and devices.^[20–22] This difference has been associated with the measurement artefacts of XRF, such as self-absorption of fluorescence photons.^[20,22] Additionally, as we are studying a compositionally complex perovskite stoichiometry (mixed cation, mixed halide), the fluorescence spectrum often contains several overlapping peaks.^[21] The aforementioned reasons reduce the accuracy of absolute elemental quantification with XRF and lead to the off-stoichiometric ratio between the lead and halides in our samples, in this case an underestimation of lead and Br. However, these experimental limitations do not affect our conclusions on the presence of Cl as the relative ratios between lead and halides are consistent across all the samples we measured. Thus, the relative evaluation between different samples should be precise and accurate as the absolute errors are equivalent. Most importantly, a Cl XRF signal was only detected in the MACl-modified samples; around 0.8 at. % of Cl with respect to the total amount of halides detected consistently in the MACl-modified samples. Hence, we can confirm that there is Cl remaining in the MACl-modified perovskite structure.

Sample Name	Pb (at. %)	I (at. %)	Br (at. %)	Cl (at. %)	I:Br:Cl ratio (%)
Control Sample 1	3.151	6.345	3.756	0	62.8:37.2:0
Control Sample 2	3.124	6.322	3.754	0	62.7:37.3:0
MACl Sample 1	3.108	6.196	3.702	0.084	62.1:37.1:0.8
MACl Sample 2	3.097	6.229	3.691	0.083	62.3:36.9:0.8

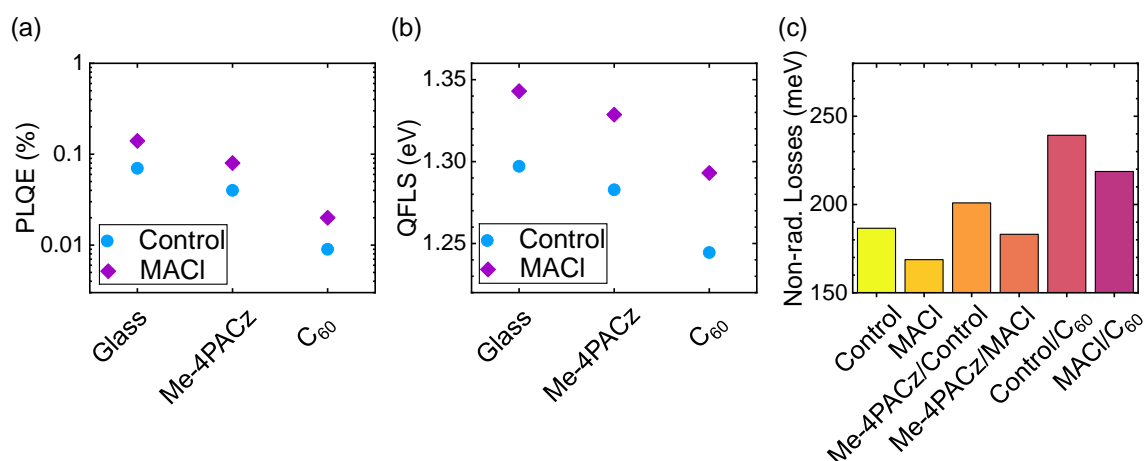
Supplementary Table 2. The atomic percentages (at. %) of the halide and the lead atoms in the $\text{FA}_{0.83}\text{Cs}_{0.17}\text{Pb}(\text{I}_{0.6}\text{Br}_{0.4})_3$ perovskite films with or without 15 mol% MACl, namely 'Control' and 'MACl' determined with Wavelength Dispersive X-Ray Fluorescence (WDXRF) measurement, as detailed in the **Supplementary Note 4**. Two samples were measured for each condition. All the samples were deposited on ITO substrates and the measured atomic percentage values have been corrected with a calibrated standard (blank ITO substrate). The I: Br: Cl ratio is calculated from the at. % of each halide.

Supplementary Note 5

To quantify the V_{oc} losses in our devices, we carried out photoluminescence quantum efficiency (PLQE) measurements on a series of perovskite ‘half-stacks’ (**Supplementary Figure 27a**). We performed these measurements on both glass substrates, to assess recombination in the isolated perovskite absorber, as well as on device half-stacks to estimate the degree of interfacial recombination at each charge transport layer/perovskite interface. As shown in **Supplementary Figure 27a**, the bare MACI-modified perovskite films on glass shows nearly 2-fold increase in PLQE compared to the control film. WBG perovskites with high Br content are known to suffer from significant non-radiative losses, often attributed to higher trap densities in the initial mixed phase.^[23,24] The enhancement in PLQE in the neat material suggests that there is reduced trap-assisted recombination in the bulk perovskite with MACI additive. This can possibly be attributed to a reduction of trap densities *via* passivating defects or improving the crystallisation process as we discuss in the main text of the manuscript. When either the HTL (Me-4PACz) or the ETL (C₆₀) are contacting the perovskite films, the PLQE is significantly reduced because of strong non-radiative recombination at both interfaces. Owing to the use of Me-4PACz, which has been shown to reduce interfacial recombination compared to other conventional polymeric transport layers,^[8,11] the PLQE losses at the HTL interface are much smaller compared with the ETL interface. Also, in this case, the MACI-modified half-stacks show higher PLQE values, indicating the formation of a better interface with both ETL and HTL.

Using the PLQE values, we can calculate the quasi-Fermi level splitting (QFLS) of the same samples and the associated non-radiative energy losses with respect to the theoretical limit of the perovskite absorber using the method as detailed in the **Supplementary Information** above (**Supplementary Figure 27a**). Consistently, the same effect can be observed in the QFLS of the MACI-modified samples, which is qualitatively in line with the higher V_{oc} achieved in our optimised perovskite solar cells. Given that the perovskite/C₆₀ interface is the most lossy interface, which results in more than 50 meV non-radiative losses, developing effective top surface passivation should be an effective strategy to reduce the V_{oc} deficit in 1.8 eV PSCs. Additionally, we also find a mismatch between the internal QFLS of the complete device stack and external open-circuit voltage (~43 meV) of our optimised devices, which is consistent with previous work using perovskites of similar bandgap and the same ETL.^[24] This

phenomenon has been associated with energetic misalignment between 1.8 eV perovskite and C₆₀.^[25] Therefore, as a future optimization, the developing of transport layers with better energy alignment will help to fully exploit the V_{oc} potential of WBG perovskites and tandem devices.



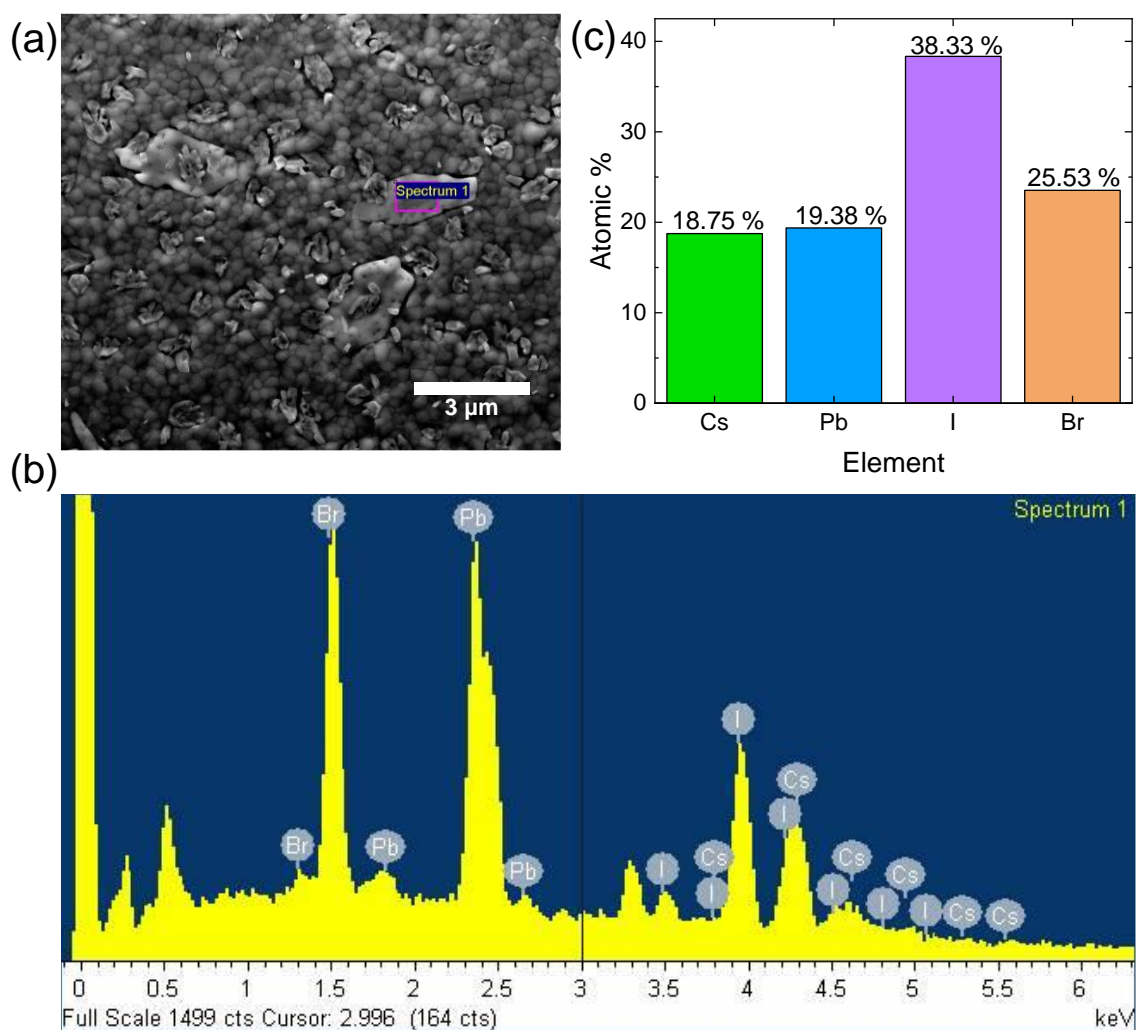
Supplementary Figure 27. (a) Photoluminescence quantum efficiency (PLQE) for bare perovskite thin-films on glass substrates, a device half-stack ITO/Me-4PACz/Al₂O₃/perovskite and glass/perovskite/C₆₀ for control and 15 mol% MACI-modified samples, namely 'MACI' and 'Control'. (b) The quasi-Fermi level splitting (QFLS) of the same samples calculated from the PLQE presented in (a) (details provided in the **Supplementary Information**). (c) Non-radiative energy losses with respect to the theoretical radiative limit of perovskite absorbers of the same samples calculated from the QFLS presented in (b) (details provided in the **Supplementary Information**).

Devices	Scan Direction	V_{oc} (V)	J_{sc} (mA cm⁻²)	FF	PCE (%)
PTAA	Reverse	1.07	17.3	0.74	13.8
	Forward	1.06	17.3	0.73	13.5
	Steady-State	1.07	16.5	0.75	13.3
Me-4PACz	Reverse	1.23	17.4	0.78	16.6
	Forward	1.21	17.4	0.77	16.1
	Steady-State	1.22	17.3	0.78	16.5
Me-4PACz + 15 mol% MACI	Reverse	1.25	17.2	0.80	17.4
	Forward	1.22	17.2	0.78	16.6
	Steady-State	1.25	17.2	0.78	17.0

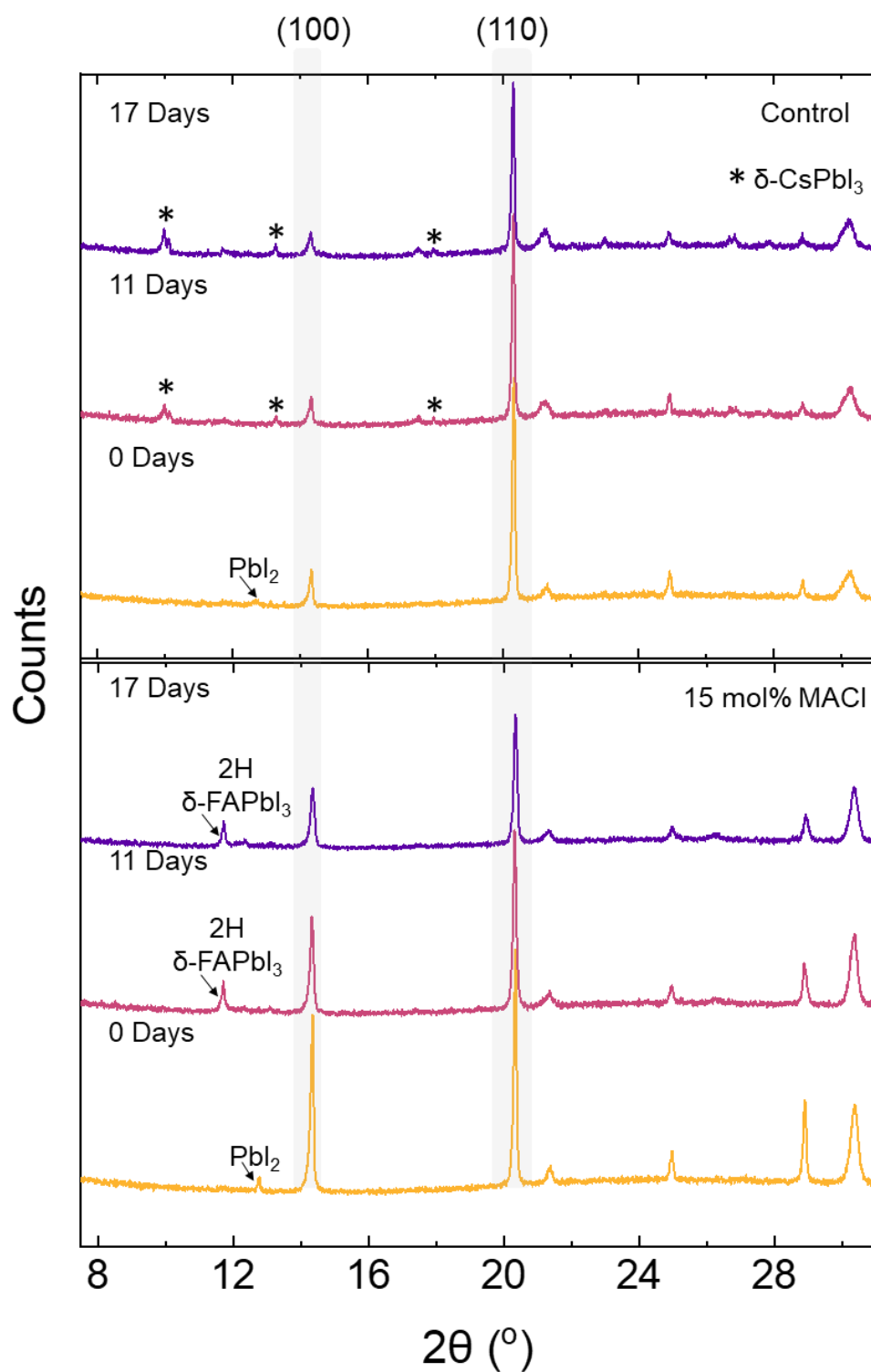
Supplementary Table 3. Device performance of the optimised perovskite solar cells. PV metrics are extracted from the J - V scan and maximum power point tracking of the champion cells ($FA_{0.83}Cs_{0.17}Pb(I_{0.6}Br_{0.4})_3$ on PTAA or Me-4PACz and $FA_{0.83}Cs_{0.17}Pb(I_{0.6}Br_{0.4})_3 + 15$ mol% MACI on Me-4PACz).

E_g (eV)	PCE (%)	V_{oc} (V)
1.81	17.1	1.21
1.80	17.2	1.266
1.80	17.7	1.26
1.80	16.3	1.21
1.80	17.4	1.25
1.79	19.3	1.33
1.79	17.8	1.26
1.77	16.5	1.216
1.77	15.9	1.206
1.76	17.3	1.22
1.75	18.3	1.26
1.73	19.07	1.25
1.72	17.1	1.24
1.715	18.9	1.35
1.71	18.5	1.21
1.71	16.74	1.24
1.70	19.2	1.20
1.68	20.8	1.23
1.67	20.4	1.22

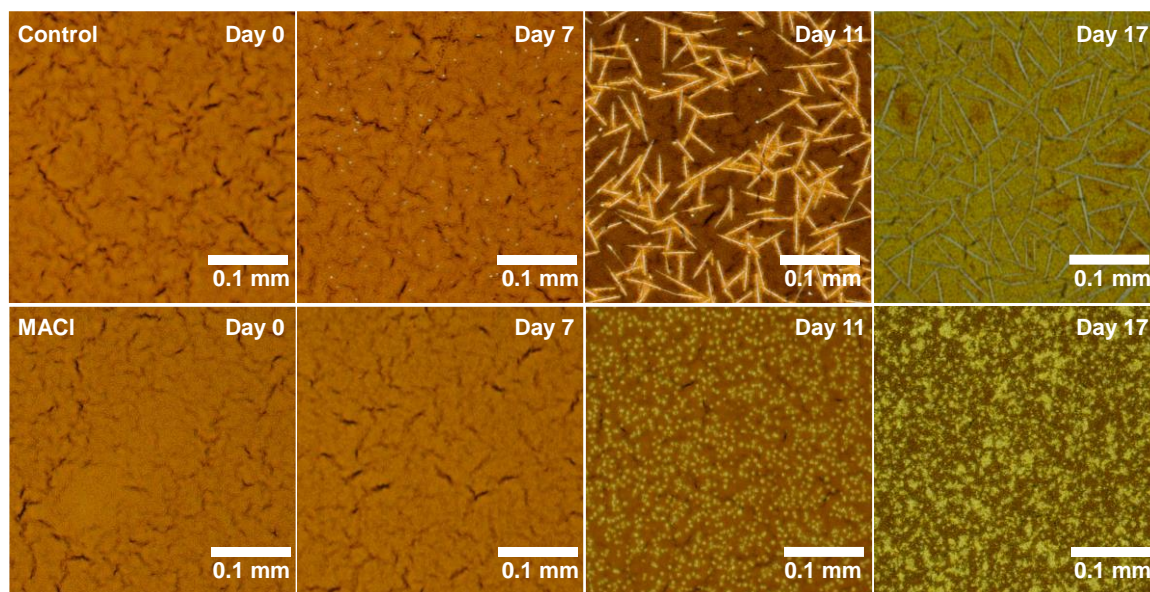
Supplementary Table 4. Device performance of high-efficiency p-i-n perovskite solar cells reported in www.perovskitedatabase.com.^[26] PV metrics are extracted from the reverse J - V scans of the champion cells. Values in bold correspond to the champion device performance report in this work.



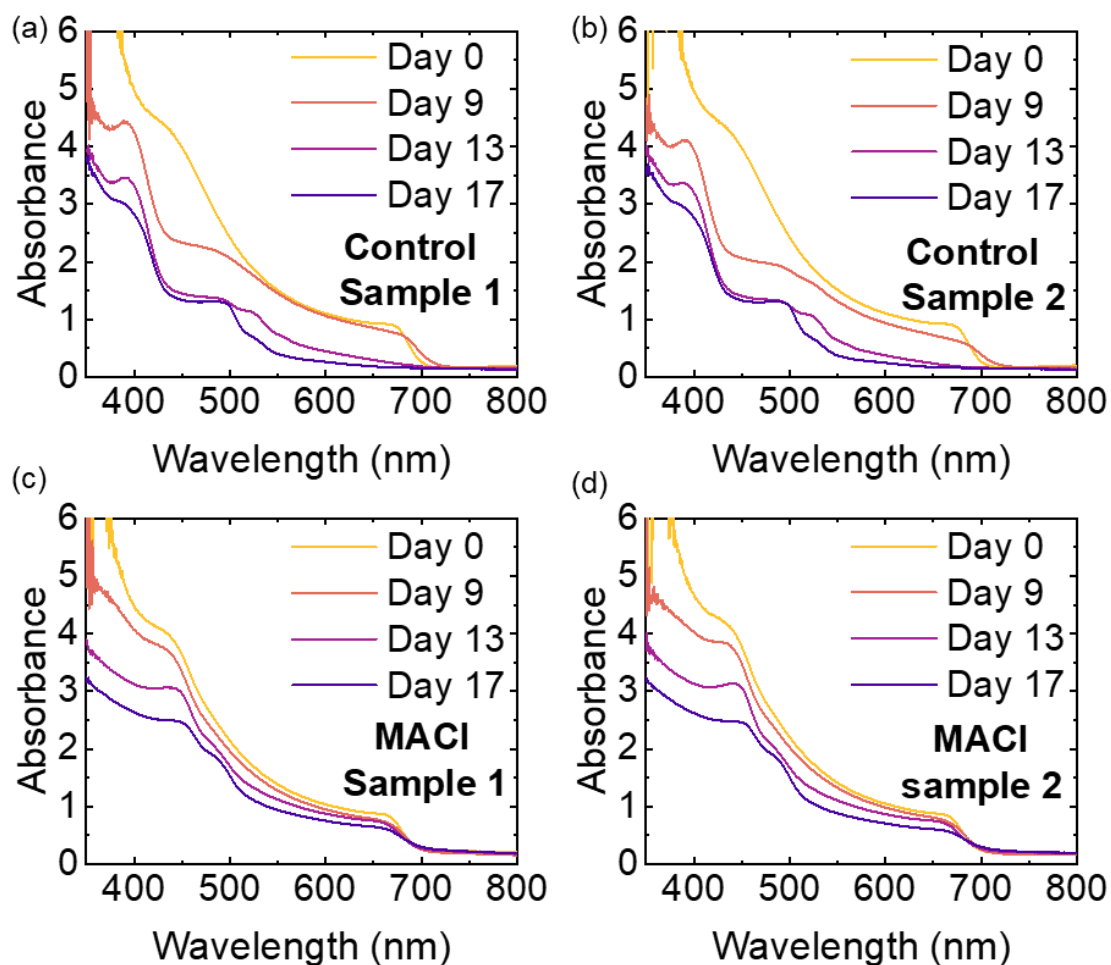
Supplementary Figure 28. Summary of energy dispersive X-ray (EDX) spectroscopy on platelets forming in degradation of control perovskite (main text **Figure 5a**). (a) Scanning electron microscopy (SEM) image of area of interest, showing region from which EDX spectrum is collected. (b) EDX spectrum, with automatic assignment of emission features applied by INCA software. (c) Chart showing atomic composition extracted from EDX spectrum (extracted using INCA software). Assignment highlights that platelet regions are Cs-rich compared to overall perovskite composition.



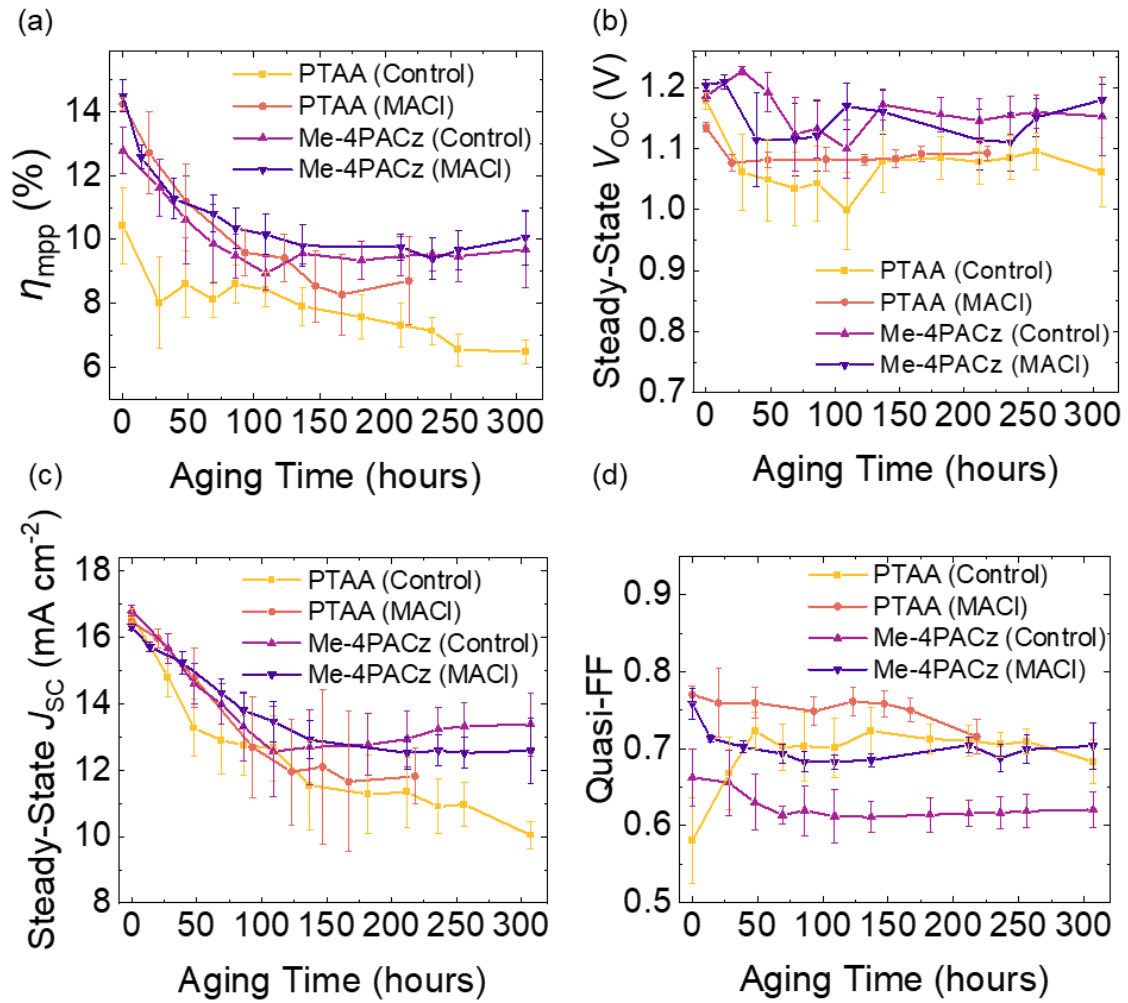
Supplementary Figure 29. Evolution of the XRD patterns of unencapsulated $\text{FA}_{0.83}\text{Cs}_{0.17}\text{Pb}(\text{I}_{0.6}\text{Br}_{0.4})_3$ films without or with 15 mol% MACl additives (denoted as 'Control' and '15 mol% MACl'), stored at dark, ambient conditions (25 °C, 50% RH in air) for 17 days.



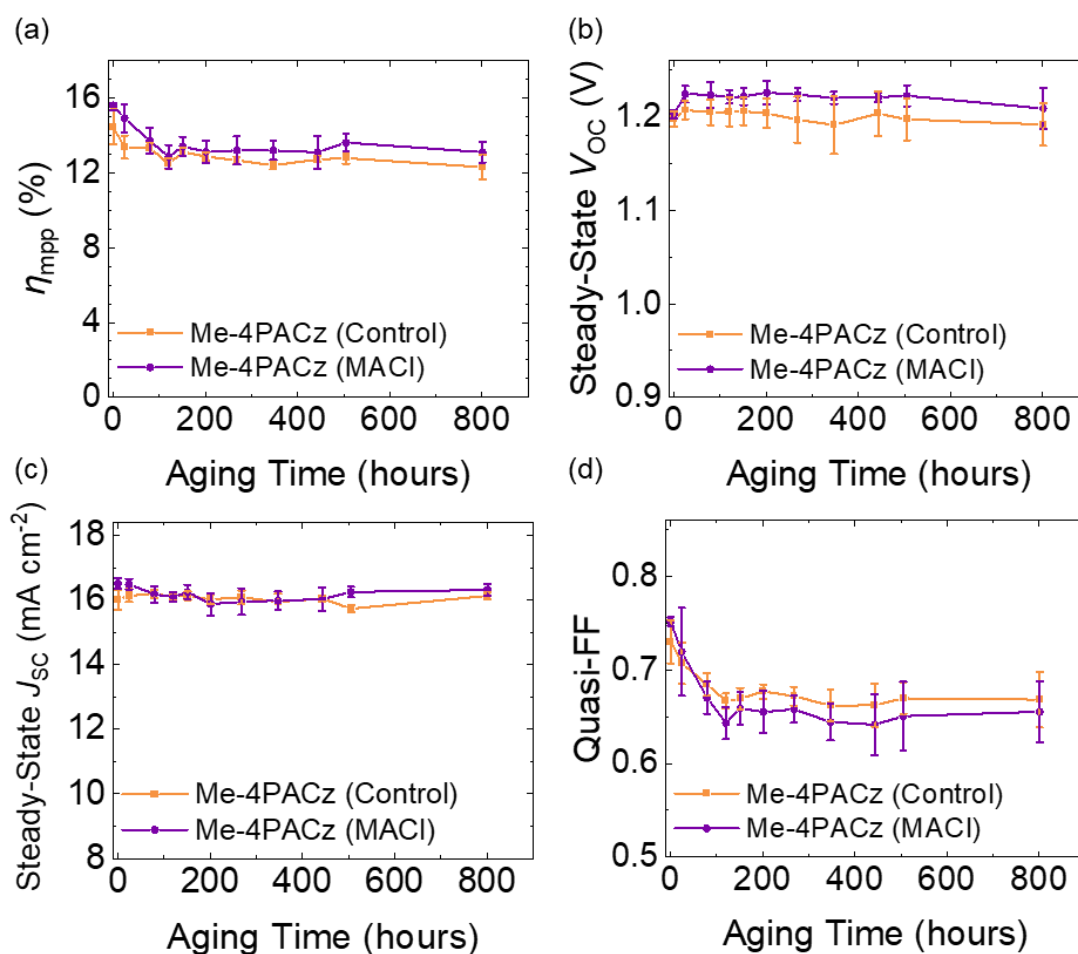
Supplementary Figure 30. Photos of unencapsulated $\text{FA}_{0.83}\text{Cs}_{0.17}\text{Pb}(\text{I}_{0.6}\text{Br}_{0.4})_3$ films without or with 15 mol% MACl additives (denoted as 'Control' and '15 mol% MACl') stored at dark, ambient conditions (25 °C, 50% RH in air) for 17 days. Photos shown here were taken with an optical microscope on Day 0, Day 7, Day 9, Day 11 and Day 17.



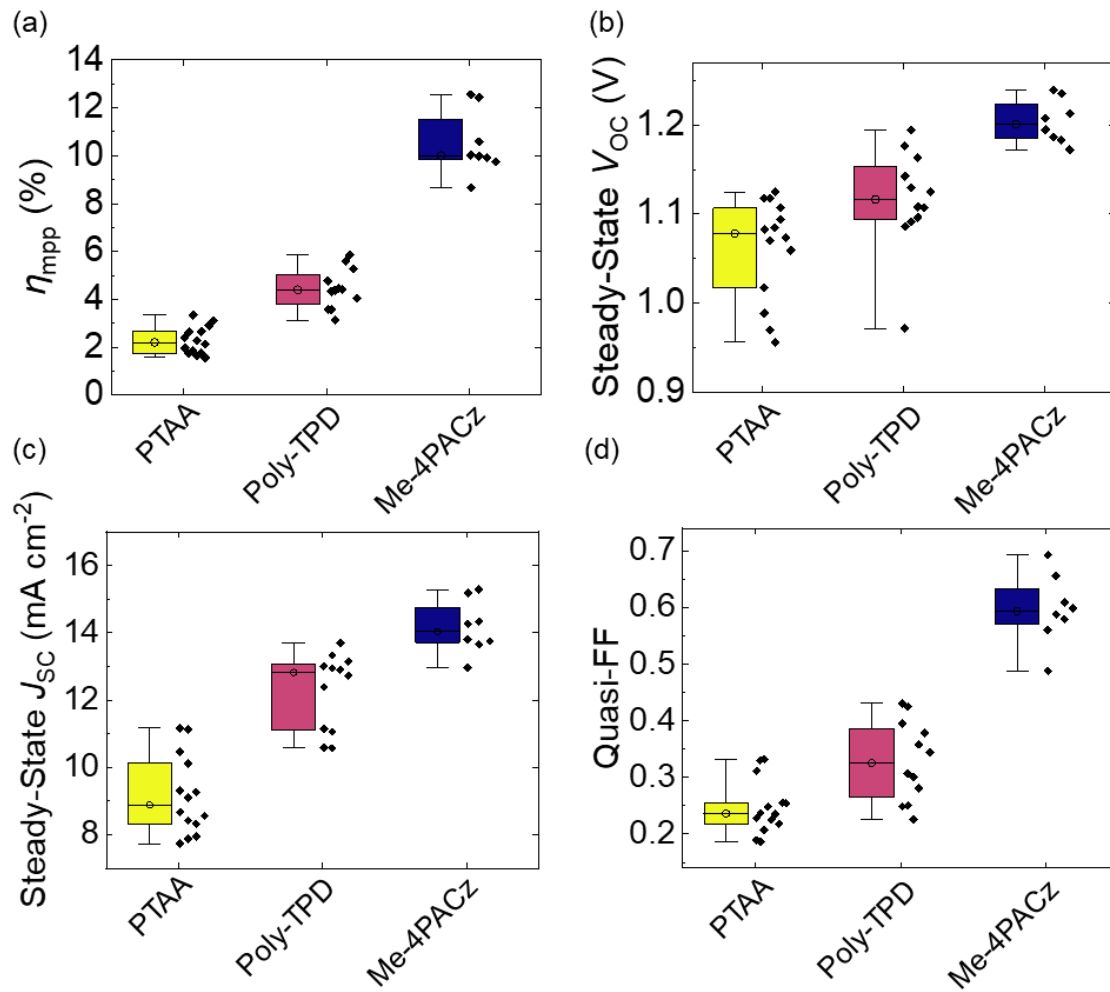
Supplementary Figure 31. Evolution of the absorbance spectra of unencapsulated $\text{FA}_{0.83}\text{Cs}_{0.17}\text{Pb}(\text{I}_{0.6}\text{Br}_{0.4})_3$ films (a – b) without or (c – d) with 15 mol% MACI additives stored at dark, ambient conditions (25 °C, 50% RH in air) for 17 days. Two samples were aged and measured for each variable, denoted as ‘Control Sample 1’, ‘Control Sample 2’, ‘MACI Sample 1’ and ‘MACI Sample 2’.



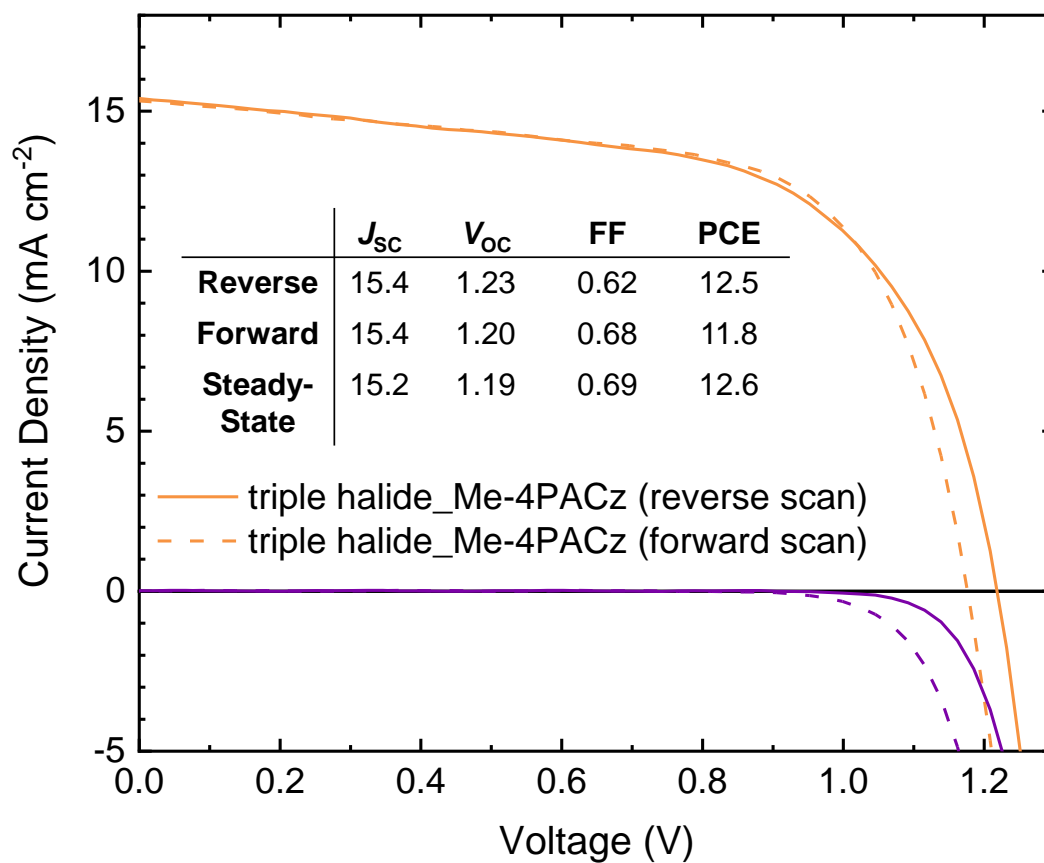
Supplementary Figure 32. Long-term photo and thermal stability measurements of encapsulated $\text{FA}_{0.83}\text{Cs}_{0.17}\text{Pb}(\text{I}_{0.6}\text{Br}_{0.4})_3$ PSCs without or with 15 mol% MAI additives based on PTAA or Me-4PACz: (a) η_{mpp} , (b) steady-state V_{OC} , (c) steady-state J_{SC} and (d) quasi-FF. All the devices were encapsulated and aged under 1-sun illumination, at open-circuit condition, 65 °C in ambient air (~ 50% RH) over 300 hours. Medians and standard median deviations of 40 devices (8-12 devices for each variable) are shown in the graph.



Supplementary Figure 33. Thermal stability measurements (η_{mpp} reported here are median of 7-8 cells of each condition from the same batch) of PSCs based on control or 15 mol% MACI-modified perovskites with Me-4PACz as the HTL and Cr/Au electrode, hence with device structure glass/ITO/Me-4PACz/Perovskite/PCBM/C₆₀/Cr/Au. The error bar is the standard deviation of 7-8 cells of each condition. All the devices were unencapsulated and aged at 85 °C, in dark, under N₂, at open-circuit condition, for over 800 hours.



Supplementary Figure 34. (a) η_{mpp} , (b) steady-state V_{oc} , (c) steady-state J_{sc} and (d) quasi-FF of $\text{FA}_{0.75}\text{Cs}_{0.25}\text{Pb}(\text{I}_{0.7}\text{Br}_{0.3})$ with 10 mol% excess of MAPbCl_3 triple halide perovskite solar cells employing PTAA, Poly-TPD and Me-4PACz respectively as hole transport layers. These devices were fabricated within one batch of experiment. Any pixel with $\eta_{\text{mpp}} \leq 75\% \eta_{\text{mpp}}$ of the champion device is cut off from the figure.



Supplementary Figure 35. *J-V* scan of the champion device based on $\text{FA}_{0.75}\text{Cs}_{0.25}\text{Pb}(\text{I}_{0.7}\text{Br}_{0.3})$ with 10 mol% excess of MAPbCl_3 triple halide perovskite solar cells with Me-4PACz as HTL.

Reference

- [1] J. Xu, C. C. Boyd, Z. J. Yu, A. F. Palmstrom, D. J. Witter, B. W. Larson, R. M. France, J. Werner, S. P. Harvey, E. J. Wolf, W. Weigand, S. Manzoor, M. F. A. M. van Hest, J. J. Berry, J. M. Luther, Z. C. Holman, M. D. McGehee, *Science* **2020**, *367*, 1097.
- [2] I. Zizak, *J. large-scale res. facil. JLSRF* **2016**, *2*.
- [3] G. Ashiotis, A. Deschildre, Z. Nawaz, J. P. Wright, D. Karkoulis, F. E. Picca, J. Kieffer, *J. Appl. Crystallogr.* **2015**, *48*, 510.
- [4] T. Dane, *A Python Library for Reduction of 2-Dimensional Grazing-Incidence and Fibre Diffraction Data*, Github, **2021**.
- [5] P. Eastman, J. Swails, J. D. Chodera, R. T. McGibbon, Y. Zhao, K. A. Beauchamp, L.-P. Wang, A. C. Simmonett, M. P. Harrigan, C. D. Stern, R. P. Wiewiora, B. R. Brooks, V. S. Pande, *PLoS Comput. Biol.* **2017**, *13*, e1005659.
- [6] P. V. G. M. Rathnayake, S. Bernardi, A. Widmer-Cooper, *J. Chem. Phys.* **2020**, *152*, 024117.
- [7] L. X. Dang, *J. Phys. Chem. B* **1999**, *103*, 8195.
- [8] P. Caprioglio, J. A. Smith, R. D. J. Oliver, A. Dasgupta, S. Choudhary, M. D. Farrar, A. J. Ramadan, Y.-H. Lin, M. G. Christoforo, J. M. Ball, J. Diekmann, J. Thiesbrummel, K.-A. Zaininger, X. Shen, M. B. Johnston, D. Neher, M. Stolterfoht, H. J. Snaith, *Nat. Commun.* **2023**, *14*, 932.
- [9] A. Dasgupta, S. Mahesh, P. Caprioglio, Y.-H. Lin, K.-A. Zaininger, R. D. J. Oliver, P. Holzhey, S. Zhou, M. M. McCarthy, J. A. Smith, M. Frenzel, M. G. Christoforo, J. M. Ball, B. Wenger, H. J. Snaith, *ACS Energy Lett.* **2022**, *7*, 2311.
- [10] R. Sitko, B. Zawisza, M. Czaja, *J. Anal. At. Spectrom.* **2005**, *20*, 741.
- [11] A. Al-Ashouri, E. Köhnen, B. Li, A. Magomedov, H. Hempel, P. Caprioglio, J. A. Márquez, A. B. Morales Vilches, E. Kasparavičius, J. A. Smith, N. Phung, D. Menzel, M. Grischek, L. Kegelmann, D. Skroblin, C. Gollwitzer, T. Malinauskas, M. Jošt, G. Matič, B. Rech, R. Schlatmann, M. Topič, L. Korte, A. Abate, B. Stannowski, D. Neher, M. Stolterfoht, T. Unold, V. Getautis, S. Albrecht, *Science* **2020**, *370*, 1300.
- [12] A. Magomedov, A. Al-Ashouri, E. Kasparavičius, S. Strazdaite, G. Niaura, M. Jošt, T. Malinauskas, S. Albrecht, V. Getautis, *Advanced Energy Materials* **2018**, *8*.
- [13] A. Al-Ashouri, A. Magomedov, M. Roß, M. Jošt, M. Talaikis, G. Chistiakova, T. Bertram, J. A. Márquez, E. Köhnen, E. Kasparavičius, S. Levenco, L. Gil-Escrig, C.

- J. Hages, R. Schlatmann, B. Rech, T. Malinauskas, T. Unold, C. A. Kaufmann, L. Korte, G. Niaura, V. Getautis, S. Albrecht, *Energy Environ. Sci.* **2019**, *12*, 3356.
- [14] M. M. Tavakoli, M. Saliba, P. Yadav, P. Holzhey, A. Hagfeldt, S. M. Zakeeruddin, M. Grätzel, *Advanced Energy Materials* **2019**, *9*.
- [15] R. Brenes, D. Guo, A. Osherov, N. K. Noel, C. Eames, E. M. Hutter, S. K. Pathak, F. Niroui, R. H. Friend, M. S. Islam, H. J. Snaith, V. Bulović, T. J. Savenije, S. D. Stranks, *Joule* **2017**, *1*, 155.
- [16] W. T. M. Van Gompel, R. Herckens, G. Reekmans, B. Ruttens, J. D'Haen, P. Adriaensens, L. Lutsen, D. Vanderzande, *J. Phys. Chem. C Nanomater. Interfaces* **2018**, *122*, 4117.
- [17] X. Wang, Y. Fan, L. Wang, C. Chen, Z. Li, R. Liu, H. Meng, Z. Shao, X. Du, H. Zhang, G. Cui, S. Pang, *Chem* **2020**, *6*, 1369.
- [18] V. Valenzano, A. Cesari, F. Balzano, A. Milella, F. Fracassi, A. Listorti, G. Gigli, A. Rizzo, G. Uccello-Barretta, S. Colella, *Cell Reports Physical Science* **2021**, *2*, 100432.
- [19] M. E. O'Kane, J. A. Smith, T. I. Alanazi, E. J. Cassella, O. Game, S. van Meurs, D. G. Lidzey, *ChemSusChem* **2021**, *14*, 2537.
- [20] M. E. Stuckelberger, T. Nietzold, B. M. West, Y. Luo, X. Li, J. Werner, B. Niesen, C. Ballif, V. Rose, D. P. Fenning, M. I. Bertoni, *J. Phys. Chem. C Nanomater. Interfaces* **2020**, *124*, 17949.
- [21] M. Kodur, R. E. Kumar, Y. Luo, D. N. Cakan, X. Li, M. Stuckelberger, D. P. Fenning, *Adv. Energy Mater.* **2020**, *10*, 1903170.
- [22] B. M. West, M. Stuckelberger, A. Jeffries, S. Gangam, B. Lai, B. Stripe, J. Maser, V. Rose, S. Vogt, M. I. Bertoni, *J. Synchrotron Radiat.* **2017**, *24*, 288.
- [23] S. Mahesh, J. M. Ball, R. D. J. Oliver, D. P. McMeekin, P. K. Nayak, M. B. Johnston, H. J. Snaith, *Energy Environ. Sci.* **2020**, *13*, 258.
- [24] R. D. J. Oliver, P. Caprioglio, F. Peña-Camargo, L. R. V. Buizza, F. Zu, A. J. Ramadan, S. G. Motti, S. Mahesh, M. M. McCarthy, J. H. Warby, Y.-H. Lin, N. Koch, S. Albrecht, L. M. Herz, M. B. Johnston, D. Neher, M. Stolterfoht, H. J. Snaith, *Energy Environ. Sci.* **2022**, *15*, 714.
- [25] M. Stolterfoht, P. Caprioglio, C. M. Wolff, J. A. Márquez, J. Nordmann, S. Zhang, D. Rothhardt, U. Hörmann, Y. Amir, A. Redinger, L. Kegelman, F. Zu, S. Albrecht, N. Koch, T. Kirchartz, M. Saliba, T. Unold, D. Neher, *Energy Environ. Sci.* **2019**, *12*, 2778.

[26] T. J. Jacobsson, A. Hultqvist, A. García-Fernández, A. Anand, A. Al-Ashouri, A. Hagfeldt, A. Crovetto, A. Abate, A. G. Ricciardulli, A. Vijayan, A. Kulkarni, A. Y. Anderson, B. P. Darwich, B. Yang, B. L. Coles, C. A. R. Perini, C. Rehermann, D. Ramirez, D. Fairen-Jimenez, D. Di Girolamo, D. Jia, E. Avila, E. J. Juarez-Perez, F. Baumann, F. Mathies, G. S. A. González, G. Boschloo, G. Nasti, G. Paramasivam, G. Martínez-Denegri, H. Näsström, H. Michaels, H. Köbler, H. Wu, I. Benesperi, M. I. Dar, I. Bayrak Pehlivan, I. E. Gould, J. N. Vagott, J. Dagar, J. Kettle, J. Yang, J. Li, J. A. Smith, J. Pascual, J. J. Jerónimo-Rendón, J. F. Montoya, J.-P. Correa-Baena, J. Qiu, J. Wang, K. Sveinbjörnsson, K. Hirselandt, K. Dey, K. Frohna, L. Mathies, L. A. Castriotta, M. H. Aldamasy, M. Vasquez-Montoya, M. A. Ruiz-Preciado, M. A. Flatken, M. V. Khenkin, M. Grischek, M. Kedia, M. Saliba, M. Anaya, M. Veldhoen, N. Arora, O. Shargaieva, O. Maus, O. S. Game, O. Yudilevich, P. Fassel, Q. Zhou, R. Betancur, R. Munir, R. Patidar, S. D. Stranks, S. Alam, S. Kar, T. Unold, T. Abzieher, T. Edvinsson, T. W. David, U. W. Paetzold, W. Zia, W. Fu, W. Zuo, V. R. F. Schröder, W. Tress, X. Zhang, Y.-H. Chiang, Z. Iqbal, Z. Xie, E. Unger, *Nat. Energy* **2021**, *7*, 107.